Xenopus cytoplasmic linker-associated protein 1 (XCLASP1) promotes axon elongation and advance of pioneer microtubules

Marx, A., Godinez, W. J., Tsimashchuk, V., Bankhead, P., Rohr, K., & Engel, U. (2013). Xenopus cytoplasmic linker-associated protein 1 (XCLASP1) promotes axon elongation and advance of pioneer microtubules. *Molecular Biology of the Cell*, *24*(10), 1544-1558. https://doi.org/10.1091/mbc.E12-08-0573

Published in:
Molecular Biology of the Cell

Document Version:
Publisher's PDF, also known as Version of record

Queen's University Belfast - Research Portal:
Link to publication record in Queen's University Belfast Research Portal

Xenopus cytoplasmic linker–associated protein 1 (XCLASP1) promotes axon elongation and advance of pioneer microtubules

Astrid Marx[a,b,*], William J. Godinez[c,*], Vasil Tsimashchuk[c], Peter Bankhead[b], Karl Rohr[a,c], and Ulrike Engel[a,b]

[a]Exzellenzcluster CellNetworks, University of Heidelberg, 69120 Heidelberg, Germany; [b]Nikon Imaging Center and Centre for Organismal Studies, University of Heidelberg BioQuant, 69120 Heidelberg, Germany; [c]Institute of Pharmacy and Molecular Biotechnology, University of Heidelberg, and Department of Bioinformatics and Functional Genomics, Biomedical Computer Vision Group, Deutsche Krebsforschungszentrum, 69120 Heidelberg, Germany

ABSTRACT **Dynamic microtubules (MTs) are required for neuronal guidance, in which axons extend directionally toward their target tissues. We found that depletion of the MT-binding protein *Xenopus* cytoplasmic linker–associated protein 1 (XCLASP1) or treatment with the MT drug Taxol reduced axon outgrowth in spinal cord neurons. To quantify the dynamic distribution of MTs in axons, we developed an automated algorithm to detect and track MT plus ends that have been fluorescently labeled by end-binding protein 3 (EB3). XCLASP1 depletion reduced MT advance rates in neuronal growth cones, very much like treatment with Taxol, demonstrating a potential link between MT dynamics in the growth cone and axon extension. Automatic tracking of EB3 comets in different compartments revealed that MTs increasingly slowed as they passed from the axon shaft into the growth cone and filopodia. We used speckle microscopy to demonstrate that MTs experience retrograde flow at the leading edge. Microtubule advance in growth cone and filopodia was strongly reduced in XCLASP1-depleted axons as compared with control axons, but actin retrograde flow remained unchanged. Instead, we found that XCLASP1-depleted growth cones lacked lamellipodial actin organization characteristic of protrusion. Lamellipodial architecture depended on XCLASP1 and its capacity to associate with MTs, highlighting the importance of XCLASP1 in actin–microtubule interactions.**

Monitoring Editor
Paul Forscher
Yale University

Received: Aug 6, 2012
Revised: Feb 19, 2013
Accepted: Mar 8, 2013

INTRODUCTION

Axon guidance is essential in the formation of the nervous system, where neurons make connections over long distances. The growth cone at the tip of the axon plays a key role in this process. This is where positional cues are perceived by membrane-associated receptors and integrated to regulate cytoskeletal dynamics (reviewed by Dent and Gertler, 2003; Lee and Van Vactor, 2003). Actin polymerization in lamellipodia and filopodia drives growth cone advance, whereas microtubules (MTs) are abundant in the axon- and the organelle-rich center of the growth cone. The interactions between actin and MTs are important for the function of both networks. During axon extension, the splayed array of MTs in the growth cone needs to be bundled (engorgement; Dent and Gertler, 2003), and this requires actin contractile structures (actin arcs; Burnette *et al.*, 2007) and MT-binding proteins (Neukirchen and Bradke, 2011). A subset of dynamic MTs, the so-called pioneer microtubules, explore the actin-rich periphery and have been studied for their role in axon guidance (Sabry *et al.*, 1991; Tanaka and Kirschner, 1991; Tanaka *et al.*, 1995; Tanaka and Kirschner, 1995; Dent and Kalil, 2001; Zhou and Cohan, 2004). Dynamic MTs in the periphery are required for adhesion (Suter *et al.*, 2004), and localized stabilization of MTs can induce growth cone turning (Buck and Zheng, 2002). Plus end–binding proteins (+TIPS) are of particular interest, as they

This article was published online ahead of print in MBoC in Press (http://www.molbiolcell.org/cgi/doi/10.1091/mbc.E12-08-0573) on March 20, 2013.

*These authors contributed equally.

Address correspondence to: Ulrike Engel (ulrike.engel@bioquant.uni-heidelberg.de).

Abbreviations used: EB3, end-binding protein 3; MT, microtubule; SIM, structured illumination microscopy; XCLASP1, *Xenopus* cytoplasmic linker–associated protein 1.

Supplemental Material can be found at:
http://www.molbiolcell.org/content/suppl/2013/03/18/mbc.E12-08-0573v1.DC1

track the growing ends of MTs and can serve as adaptors for actin-binding proteins (reviewed by Akhmanova and Steinmetz, 2008; van der Vaart *et al.*, 2009).

Orbit/MAST, one of the +TIPS originally identified by its mitotic phenotype (Inoue *et al.*, 2000; Lemos *et al.*, 2000), is involved in axon guidance in *Drosophila* (Lee *et al.*, 2004). Orbit's homologues in vertebrates are the cytoplasmic linker protein-associated proteins 1 and 2 (CLASP1/2; Akhmanova *et al.*, 2001), which have been shown to regulate MT dynamics selectively at the cell periphery of HeLa cells (Mimori-Kiyosue *et al.*, 2005) and stabilize MTs close to focal adhesions (Lansbergen *et al.*, 2006). In neurons, a recent study highlights a dual role for CLASP in promoting or inhibiting axon extension dependent on the levels of GSK-3 (Hur *et al.*, 2011). Whereas in other vertebrates the redundancy between CLASP1 and 2 complicates analysis, in *Xenopus* there is only one CLASP, which is a homologue of vertebrate CLASP1 (Hannak and Heald, 2006), referred to in this article as *Xenopus* cytoplasmic linker–associated protein 1 (XCLASP1).

For many MT-binding proteins a role in axon outgrowth has been established; however, our understanding of the precise role of MT dynamics in this process is limited. This is partly due to the lack of methods to quantify MT dynamics in neurons. When MTs are labeled by fluorescent tubulin, analysis of MT dynamics is limited to regions of low MT density (e.g., the periphery) and relies on manual tracking (Tanaka and Kirschner, 1991; Tanaka *et al.*, 1995; Tanaka and Kirschner, 1995; Dent and Kalil, 2001; Komarova *et al.*, 2002). Detection of +TIPS to highlight growing MTs has been successfully used in neurons (Stepanova *et al.*, 2003; Lee *et al.*, 2004; Ma *et al.*, 2004).

The need for automated tracking approaches has been widely recognized, and automated tracking programs for +TIPS have been developed and used in epithelial cells (Matov *et al.*, 2010; Applegate *et al.*, 2011). Automation is required because of the stochastic nature of MT dynamics (Mitchison and Kirschner, 1984), which demands the analysis of many tracks to analyze knockdown phenotypes (Nishimura *et al.*, 2012). In neurons, semiautomated tracking of end-binding protein 3 (EB3) comets along neurites based on kymographs was used by Stepanova *et al.* (2010). This approach was successful for the axon shaft, where the comets follow a predetermined direction. In growth cones, dynamic MTs follow individual, curved tracks, and an alternative solution is therefore required.

We developed automated tracking of MT plus ends in growth cones to examine CLASP's role in MT dynamics and axon outgrowth in embryonic spinal cords of *Xenopus laevis*. We used low-level expression of fluorescent +TIP EB3 (Stepanova *et al.*, 2003, 2010) and low–temporal resolution time lapse compatible with extended imaging of neurons. We found that XCLASP1 promotes axon extension and is a positive modulator of MT plus ends in the growth cone. Similar to XCLASP1 depletion, Taxol reduced EB3 comet velocities, underlining the importance of MT dynamics for growth cone advance. In addition to its role in the regulation of pioneer MTs, we found XCLASP1 to be important for lamellipodial actin architecture.

RESULTS

XCLASP1 is up-regulated during axon outgrowth and promotes axon extension

In situ hybridization revealed that the mRNA expression of XCLASP1 in the nervous system was developmentally regulated. In stage 28 embryos, XCLASP1 mRNA was strongly enriched in spinal cord, spinal cord motor neurons, and cranial nerves (Figure 1A; Park *et al.*, 2012). In the fully motile tadpoles of stage 41, XCLASP1 mRNA could no longer be detected by in situ hybridization (Figure 1, compare B and C). This pattern suggests that XCLASP1 is up-regulated in spinal cord and other motor nerves during their development and decreases dramatically after axon outgrowth is completed. An antibody against XCLASP1 (Xorbit antibody; Hannak and Heald, 2006) recognizes XCLASP1 in growth cones of stage 28 embryos, where it localizes to MT tips and only to a lesser extent along the MT shaft (Figure 1D). This distribution is mimicked by enhanced green fluorescent protein (EGFP)–XCLASP1ΔN (Supplemental Movie S1) and resembles the localization of human EGFP-CLASP2γ (Figure 2A; Lee *et al.*, 2004).

To investigate the role of XCLASP1 in axon outgrowth, we used a loss-of-function approach. We depleted XCLASP1 selectively in the nervous system by injecting a morpholino oligonucleotide (XCLASP1 MO) into the early embryo (see *Materials and Methods*). Efficiency of depletion was confirmed by immunocytochemistry in neurons (Supplemental Figure S1A) and by Western analysis in *Xenopus* epithelial cells (Supplemental Figure S1B). Neuronal outgrowth rates were significantly reduced in XCLASP1 knockdown cultures (Figure 1E). Of interest, when comparing the growth path to the direct distance from origin to end of the track, we detected increased curved outgrowth for XCLASP1-depleted axons (see later discussion of Figure 6F). Low concentrations of Taxol likewise decreased axon extension and resulted in a loss of growth directionality (Figure 1, G and H). Because both depletion of the +TIP CLASP and the microtubule drug Taxol resulted in attenuated axon extension, we wanted to investigate how MT dynamics and growth cone advance are related.

Automated MT plus-end tracking in neuronal growth cones allows analysis of large data sets

To analyze MT dynamics in growth cones, we used EB3-EGFP or EB3-mCherry to visualize growing MT plus ends in *X. laevis* spinal cord growth cones (Figure 2, A and C). EB1 and EB3 are well-known markers for growing MTs (Mimori-Kiyosue *et al.*, 2000; Stepanova *et al.*, 2003; Morrison, 2007). To gauge expression levels, we compared EB3-mCherry signal (Figure 2C) to the endogenous pattern of EB1 as detected by a commercial antibody (Figure 2B). The expression resulting from injection of EB3-EGFP or EB3-mCherry capped mRNA (*see Materials and Methods*) resulted in the same pattern as observed for the endogenous EB1. We found that EB3 fused to fluorescent proteins localized on MT plus ends, where it localized in a comet-like manner. This is in contrast to EGFP-CLASP2γ expressed in *X. laevis* neurons, which we found to localize also to the MT lattice (Figure 2A; Lee *et al.*, 2004). EB3-mCherry localized to plus ends in growth cone and shaft (Figure 2A), as did EGFP-CLIP-170, whereas CLASP2γ showed a preference for growth cone MTs (Figure 2A; Lee *et al.*, 2004). We therefore used EB3-mCherry at low expression for MT plus-end visualization (Figure 2C and Supplemental Movie S2). EB3-mCherry comets can be clearly separated from each other, and single MT plus ends can be followed over many frames (Figure 2D, arrow, and Supplemental Movie S2).

To quantify the MT dynamics in wide-field fluorescence time-lapse sequences, we developed a probabilistic approach for tracking EB3 comets in movies with very moderate temporal resolution (one image every 3 s). To localize comets within an image, we used an approach based on two-dimensional (2D) Gaussian fitting (Wörz *et al.*, 2010). The positions over time of the individual comets were estimated using an approach based on Kalman filters (Godinez *et al.*, 2009; see *Materials and Methods* for detailed description).

When we compared all the tracks visible in the image sequence to the tracks that were automatically recognized (Figure 2E, green lines) it became evident that the majority of tracks were recognized,

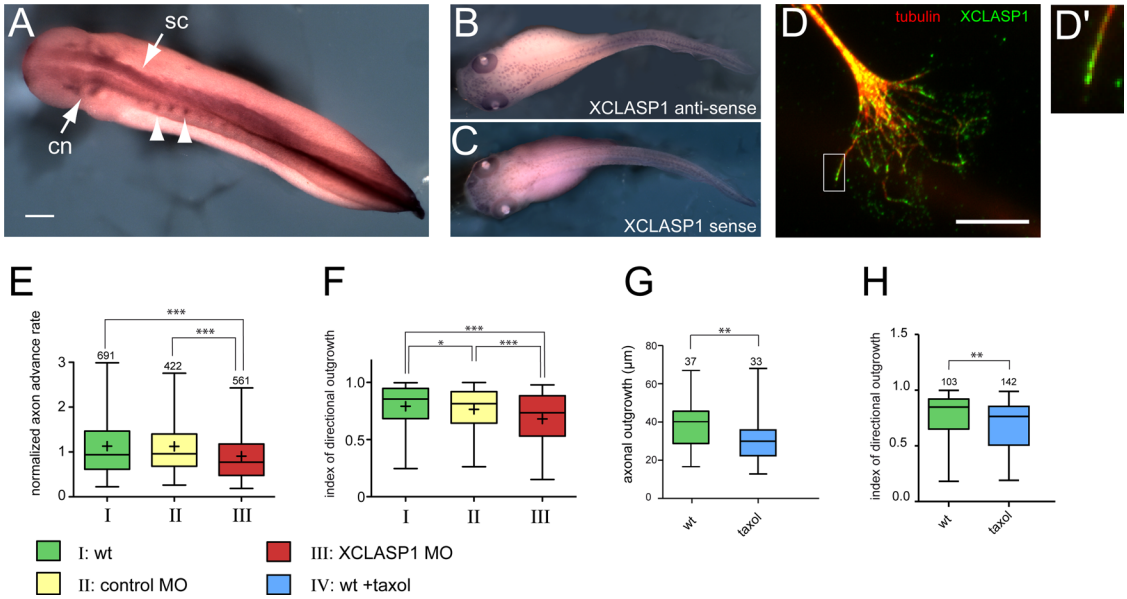

FIGURE 1: XCLASP1 depletion in spinal cord neurons results in reduced axonal outgrowth. (A) In situ hybridization of XCLASP1 riboprobe reveals localization of XCLASP1 mRNA expression in longitudinal fascicles of the spinal cord (sc), axons of motor neurons (arrowheads), and cranial nerves (cn) in stage 28 embryos. Scale bar, 200 µm. (B, C) In situ hybridization of XCLASP1 in stage 41 embryos with antisense (B) and sense (C) riboprobe. Dark speckles represent melanocytes in the skin. (D) XCLASP1 localizes to MT plus ends in neuronal growth cones as detected by Xorbit antibody. Scale bar, 10 µm. (D′) Magnified view of the boxed region in D. (E) Axon elongation rates of spinal cord neurons (I; wild type [wt]) injected with control morpholino (II; control MO) and morpholino directed against XCLASP1 (III; XCLASP1 MO). Instantaneous outgrowth velocities were averaged per track, and four independent experiments are summarized by normalization to the wt median. The number of analyzed tracks is indicated. (F) To calculate the index of outgrowth directionality, the distance from origin to end of the path was divided by the path length for the tracks analyzed in E. (G) Axonal outgrowth after low-dose application of Taxol (7 nM) added 40 min before imaging. Axonal outgrowth during 30 min is expressed as the path length. The number of tracks analyzed is indicated. (H) Index of outgrowth directionality (see F) calculated for axon outgrowth shown in G. Box plots extend from 25th to 75th percentile, error bars from 2.5th to 97.5th percentile, and the median is indicated as a horizontal line and the mean as a cross. ***$p < 0.0001$, **$p < 0.01$, *$p < 0.05$.

although not all. The efficiency of tracking was 83% in the shaft and 78% in the growth cone (n = 13 time-lapse sequences). The automated tracking allows us to determine direction and instantaneous and average velocities, as well as track length and duration. The histogram of the growth rate in wild-type *X. laevis* growth cones (Figure 2F) indicates that the velocities approximately follow a Gaussian distribution, with a mean velocity of 7.16 ± 3.7 µm/min (n = 269 tracks in eight time-lapse sequences). The mean comet lifetime is 23.76 s, but 11.7% of the tracks are also in the range of 42–60 s (Figure 2G). Here we define comet lifetime as the period in which the tracking algorithm could follow a single EB3-EGFP comet. When the EB3 label is lost upon pausing or shortening, this results in the track stopping. Although we cannot determine all classic MT dynamic instability parameters directly using a +TIP, lifetimes give us an indication about transitions from polymerization to pause or catastrophe.

Given that the automatic tracking recognizes a subset of all tracks, we compared the results of our automated tracking approach (Figure 2, A and B) by manual kymograph analysis. When we analyzed all tracks of a 5-min-long sequence, we found that the velocities of all the 62 tracks found manually and measured by kymograph analysis (see Supplemental Figure S2) are not significantly different from the subset of 46 tracks found automatically (Figure 3A). When just comparing results from those 46 tracks that were analyzed both manually and automatically, we found that the resulting velocities were almost identical (6.98 ± 2.34 µm/min in automated tracking and 6.99 ± 2.37 µm/min in kymograph; Figure 3A).

Finally, when we verified our tracking on a wider range of image sequences, we compared the mean velocities of 244 tracks obtained in 37 sequences with the results obtained by kymograph analysis in the same sequences. Comparing results, we did not find a significant difference (Figure 3B), demonstrating that our automated tracking of EB3-EGFP comets is a reliable method to assess MT dynamics.

Our mean MT advance rates are lower than reported earlier for *Xenopus* growth cones (Lee *et al.*, 2004). In three independent experiments in this study, mean plus-end velocities differed by around 2 µm/min (Table 1). Frog cultures are kept and imaged at room temperature, which is not tightly controlled and can change MT dynamics. For statistical analysis data from different days was therefore normalized to the wild-type values of a given day.

We also wondered whether short pauses contributed to lower average velocities. When we analyzed instantaneous velocities, these rarely dropped to <1 µm/min within a track (nine events in 560 tracks).

Low Taxol concentration and XCLASP1 depletion reduce MT dynamics and axon outgrowth

Taxol-treated neurons showed decreased axon extension similar to XCLASP-depleted neurons. We therefore sought to learn how

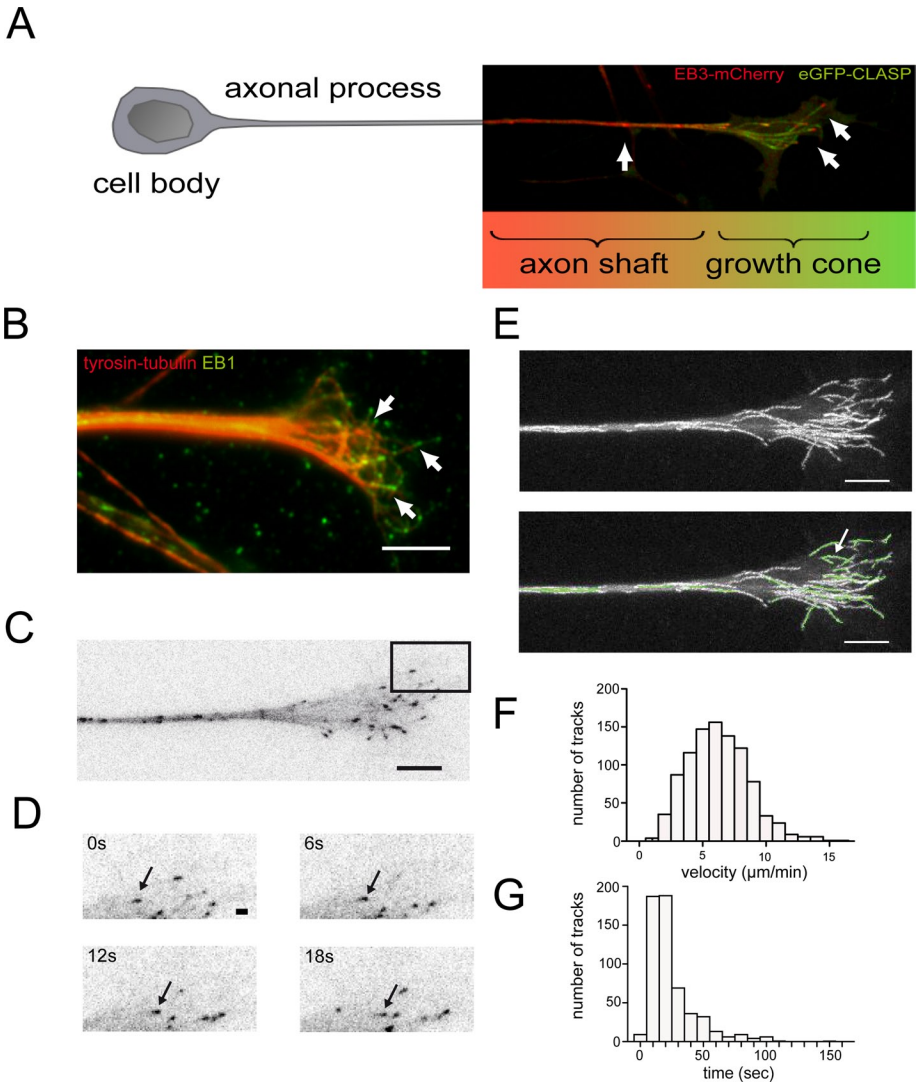

FIGURE 2: Automated tracking of EB3-mCherry comets in *Xenopus* neuronal growth cones. (A) Expression of EGFP-CLASP2γ and EB3-mCherry. EB3-mCherry highlights MT plus ends in growth cone and shaft (arrows), EGFP-CLASP2γ is enriched in the growth cone and also shows lattice binding. (B) EB1 and tyrosine-tubulin antibody staining. EB1-positive comets are marked by arrows. (C) EB3-mCherry expression in neuronal growth cone and shaft. The mCherry signal is shown intensity inverted. (D) Time-lapse of boxed region in C. Arrow marks a comet that can be followed through the image sequence. (E) Maximum-intensity projection through time (25 frames, 75 s). EB3-mCherry comets highlight tracks of MT plus ends. Bottom, superimposition of tracks generated by automated tracking (green). Arrow indicates track shown in D. (F) Distribution of EB3 comet displacement rates; the mean is 7.15 µm/min (269 EB3-mCherry tracks, eight neurons). (G) Distribution of track lifetimes; the mean is 20.93 s (269 EB3-mCherry tracks, eight image sequences). Scale bars, 5 µm (B, C, and E), 1 µm (D).

axonal outgrowth was connected to MT dynamics. In Taxol-treated spinal cord cultures, we detected a dose-dependent reduction of plus-end advance in the growth cone (Figure 3, C and D). Motile EB3 comets are visible with up to 10 nM Taxol (Supplemental Movie S3), demonstrating that polymer is still added at this concentration. Using automatic tracking of plus ends, we observed that 2.2 nM Taxol was the concentration that had a half–maximal effect (IC_{50}) on advance of growth cone MTs (Figure 3D). Track length was approximately halved (Figure 3E), whereas track lifetime was unaffected by concentrations up to 3.3 nM and only decreased marginally at high concentrations (Figure 3F). In summary, Taxol at <10 nM concentration reduced axon outgrowth and MT advance in *Xenopus* spinal cord neurons.

When we analyzed MT plus-end dynamics by automated tracking in XCLASP1-depleted growth cones, we detected that MTs in XCLASP1 knockdown growth cones had reduced velocities compared with control morpholino and wild type (Figure 4A). This was due to a significant decrease in track lengths (Figure 4B), whereas comet lifetimes were even slightly increased (Figure 4C). In an experiment that directly compared morpholino-injected neurons to those with Taxol treatment, the plus-end velocity was shifted to 5 µm/min for both Taxol treatment and XCLASP1 depletion, whereas MT velocities of control morpholino and untreated neurons in the growth cone peaked around 6–7 µm/min (Figure 4D). Although we see differences in the way Taxol affects lifetimes, Taxol and XCLASP1 both reduce pioneer MT advance into the growth cone periphery, and this is correlated with decreased axon extension (Figure 1, E and G). The sustained lifetime in XCLASP1-depleted cells points to fewer transitions to catastrophe or pause. In the context of growth cone morphology, this suggests that in XCLASP1-depleted cells, most plus ends travel to the growth cone periphery before catastrophe occurs but need more time to reach it. In addition to reduced growth, MT plus ends followed more curved routes in XCLASP1-depleted growth cones, resulting in less directional advance of MTs into the periphery (Figure 4E).

MT dynamics differs in axon shaft, growth cone, and filopodia

In the axon, MTs are aligned parallel to one another and polymerization occurs mainly in the anterograde direction (Stepanova *et al.*, 2003, 2010). MTs in the axonal shaft therefore grow predominantly in direction of the growth cone and pass the growth cone neck, where they splay out and grow at different angles toward the periphery (Supplemental Movie S2). We sought to investigate the difference in dynamics of MTs in the axon and subcompartments of the growth cone. On the basis of the stereotypical behavior of MT ends advancing from the growth cone center to the periphery (see tracks in Figure 2C and Supplemental Movie S2), we first used a very simple method to obtain information about MT behavior in the periphery. We analyzed the life histories of tracks. Starting from the end of the track (catastrophe or pause), we compared the final five frames with the five frames before them. The velocity of the five last frames was on average 12% lower than that of the previous frames (Supplemental Table 1), indicating that in the growth cone transition to catastrophe or pause is preceded by a reduction in advance rate. In the axon shaft, the same analysis showed that MTs slowed by only 5% or less in their final five frames before disappearance of

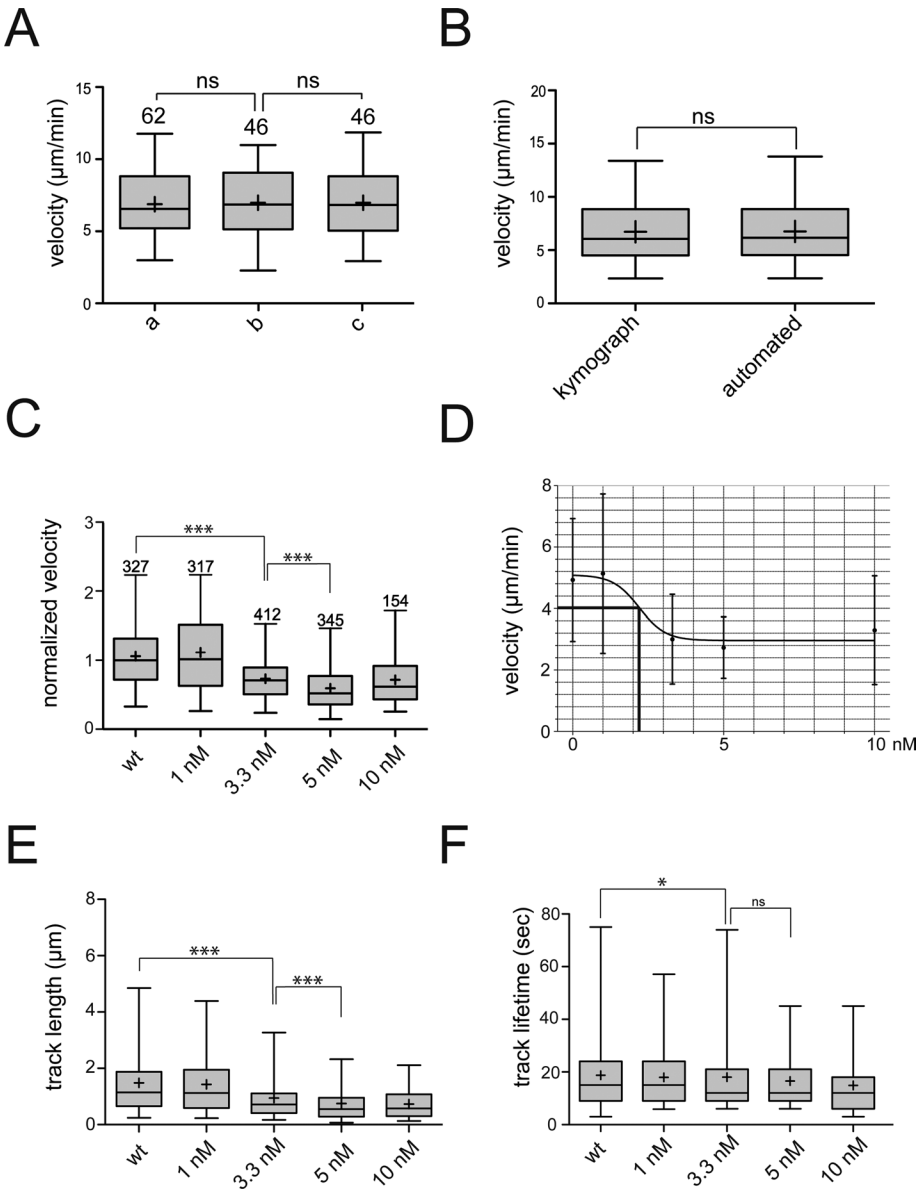

FIGURE 3: Taxol reduces velocities of EB3-EGFP comets. (A) Comparison of plus-end velocities obtained from manual and automated tracking. Sixty-two EB3-EGFP comets in one image sequence were manually tracked and analyzed using kymographs (see Supplemental Figure S2). The resulting velocities (a) were compared with the velocities of tracks also identified by manual (b) and automated tracking (c). These groups show no significant difference (ns) in their velocity distribution. (B) Velocity distribution in 244 tracks from 37 growth cones that were analyzed by tracking or automated tracking. Comparison between these groups reveals no significant difference. (C) Plus-end velocities of EB3-EGFP in growth cones at different Taxol concentrations were evaluated and normalized against the wt median. Values are from $n = 2$ experiments, and the number of analyzed tracks is indicated (and is the same for C–E). (D) Mean velocities with SD of tracks were plotted against the Taxol concentrations, and a curve was fitted to determine the IC_{50} (2.2 nM). (E, F) EB3-EGFP track length (E) and lifetime (F) in the growth cone. Box plots as in Figure 1. ***$p < 0.0001$, **$p < 0.01$, *$p < 0.05$.

the comet (Supplemental Table 1), in agreement with findings in hippocampal axons (Stepanova *et al.*, 2010).

To learn how MT behavior correlated with MT-actin interaction, we imaged EB3-mCherry together with Lifeact-EGFP (Figure 5 and Supplemental Movie S4), where Lifeact visualizes F-actin (Riedl *et al.*, 2008). Actin structures localize predominantly to filopodia and lamellipodia in the periphery. (Figure 5, A and B, schematic). A typical example of an EB3 track passing from a region of low actin density into the actin-rich periphery is shown in detail in Figure 5D. After 18 s of growth, the track reaches a strong actin bundle at an angle of nearly 90°. The MT stops growing and intermittently loses the EB3-mCherry signal in the next frame. The effect of coupling to actin is visible in the velocity profile (Figure 5F): on contact with the bundle, there is a marked decrease in advance rates in the following time frames.

MT plus ends often enter the base of filopodia (Figure 5E; quantitation in Supplemental Table 2; Lee *et al.*, 2004); however, when they do so, we always observed a decrease in advance rate (Figure 5G). To quantify MT growth rate changes induced by filopodia interactions, we developed an algorithm that automatically recognizes filopodia based on segmenting them as thin lines (Figure 5C; see *Materials and Methods*). This dynamic segmentation was then combined with our tracking software to divide tracks within the growth cone into two parts: the part where the EB3-EGFP tracks grow inside the central region, and the part after they enter filopodia. Our analysis in wild-type neurons revealed that MTs in the axonal shaft of wild-type neurons exhibit the highest growth velocity, with a mean of 10.2 µm/min, which decreased to 8.9 µm/min in the growth cone. When the plus ends entered filopodia they further slowed to 8.0 µm/min (Figure 5H). These changes in velocity were visualized by assigning a color code to individual tracks (Figure 5I; see Supplemental Movie S5). In XCLASP1-depleted neurons, comet velocities were significantly decreased compared with wild type and control morpholino in all compartments; however, the difference was most pronounced in the

Treatment	Experiment 1		Experiment 2		Experiment 3	
	wt	XCLASP1 MO	wt	XCLASP1 MO	wt	XCLASP1 MO
Number of tracks analyzed	269	385	560	728	647	532
Comet velocity in growth cone (µm/min ± SEM)	7.2 ± 0.17	5.4 ± 0.14	10.5 ± 0.17	6.1 ± 0.10	9.6 ± 0.15	8.1 ± 0.15

TABLE 1: Variation of comet velocities in growth cones.

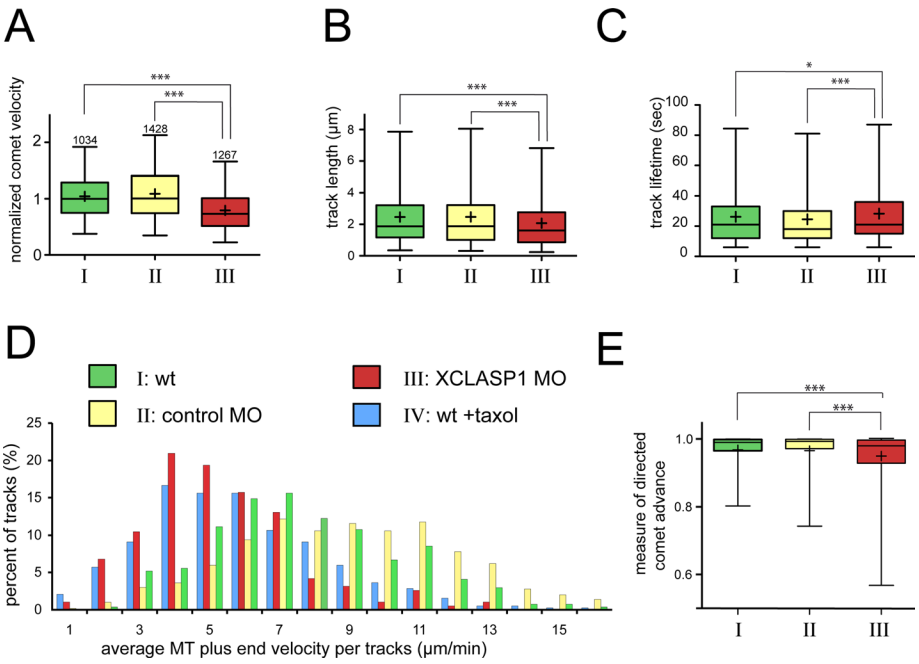

FIGURE 4: Pioneer MTs in XCLASP1-depleted growth cones show slower advance rates. (A–C) Analysis of plus-end dynamics in spinal cord growth cones by automated tracking of EB3-comets. The results of three experiments were normalized to the wt medians of each experiment, and the number of analyzed tracks for A–C is indicated in A. (A) Velocities of EB3 comets in growth cones. Statistics were calculated from average velocity per track. (B) Track length of EB3 tracks in the growth cone. (C) Corresponding lifetimes of EB3 tracks. (D) Histogram of EB3 comet velocities for growth cones of spinal cord neurons injected with control morpholino (II; control MO), a morpholino directed against XCLASP1 (III; XCLASP1 MO), uninjected neurons (I; wt), and neurons treated with 7 nM Taxol for 40 min (IV; wt + Taxol). Average velocities per track are summarized in bins of multiples of 1 µm/min. (E) Track curvature was taken as a measure of directed comet advance. It was calculated by the distance connecting origin and end of track divided by the total track length. Box plots as in Figure 1. ***$p < 0.0001$, *$p < 0.05$.

growth cone and less pronounced in the shaft. The analyzed shaft in these experiments comprised only the first 50 µm closest to the growth cone because our field of view was limited by the objective and camera we used for EB3 imaging. To overcome this restriction, we conducted an additional study with a large camera sensor, which allowed us to image up to 150 µm of the shaft in addition to the growth cone (Figure 5J and Supplemental Movie S6). Indeed, when we compared the closest 40 µm of shaft (proximal) with the more distant part (distal; Figure 5J) we observed that plus-end tracks picked up speed as they approached the growth cone and then slowed strongly in the periphery of the growth cone (Figure 5K). In XCLASP1-depleted axons, this behavior differed, as plus-end velocities changed less as plus ends passed from the distal part of the axon to the growth cone and then slowed further in filopodia (Figure 5K). This suggests that XCLASP1 regulates MT dynamics in and near the growth cone but not in the axon closer to the cell body.

MTs undergo anterograde movement in the shaft and can couple to retrograde flow in the periphery

The reduced displacement rates of EB3 in the growth cone periphery and in filopodia could be caused by changed regulation of polymerization or physical coupling with actin retrograde flow. Association of EB3 with slow-growing plus ends argues for the MT to be still polymerizing; however it is impossible to decide whether decreased advance is caused by reduced polymerization or backward movement of the polymer.

To gain insight into whether MT polymer transport was involved, we injected embryos with low concentrations of HiLyte488-tubulin or EGFP-tubulin and used the uneven incorporation of fluorescent tubulin to visualize speckles of labeled tubulin in the polymer (speckle microscopy; Waterman-Storer and Salmon, 1998). This analysis was easiest to perform in the actin shaft because the abundance of polymer there provides good signal even at low tubulin concentrations. Of 24 examined spinal cord axons, 15 showed anterograde polymer transport up to 3 µm/min, whereas nine showed no net transport. The only instance in which we observed retrograde transport in the shaft was when a growth cone collapsed and the axon retracted. In the shaft both speckle movement and plus-end movement could be measured by kymograph analysis (Figure 6, C and D). By concurrent analysis of EB3 comet displacement and MT flow in the shaft of 10 axons, we detected a correlation between speckle advance and MT displacement (Figure 6E). Forward movement of MT polymer was described for *Xenopus* axons before and linked to active forward movement of the growth cone (Chang *et al.* 1998, 1999).

Assessment of polymer transport in the growth cone proved much more difficult because MTs undergo individual fates, and the outline of MTs is hard to identify with low label incorporation. In most growth cones, anterograde transport of MTs seemed to continue in the central domain of the growth cone (Figure 6D and Supplemental Figure S3B). In growth cones we observed MTs at the periphery that exhibited retrograde transport of several micrometers/minute (Figure 6, H′ and J′). Some of these MTs were polymerizing while being transported backward, as revealed by EB3 comets in the same sequences (Figure 6, H–J). It became clear that stationary EB3 comets at the periphery (Figure 6I) were in a tug of war between retrograde transport and forward movement by polymerization (Figure 6, J, J′, and J″). We measured rates of MT backward flow up to 5–6 µm/min (Figure 6, H′ and J′; see also Supplemental Figure S3, D and E) with a sharp transition in the central domain, where retrograde flow was almost completely attenuated (0.8 µm/min; Figure 6H′). In the case of the EB3 comet that stayed for 12 s at the periphery (Figure 6I, d), the retrograde flow visible on the MT was around 5 µm/min (Figure 6J′) indicating that what looks like pausing is the net outcome of tubulin addition and polymer movement in the opposite direction. In these experiments we could not introduce an additional label to trace actin retrograde flow, but our measurement of actin retrograde flow in the growth cone periphery in parallel experiments show rates that are in agreement with the observed MT transport (4.2 ± 2.8 µm/min; Figure 6K). Our results indicate that MT coupling to actin in the periphery may contribute to slowed advance of MTs in the periphery.

When we quantified actin retrograde flow in XCLASP1-depleted growth cones, there was little difference between XCLASP1-depleted growth cones and control (Figure 6K), and the difference was not sufficient to explain the decreased advance of pioneer MTs

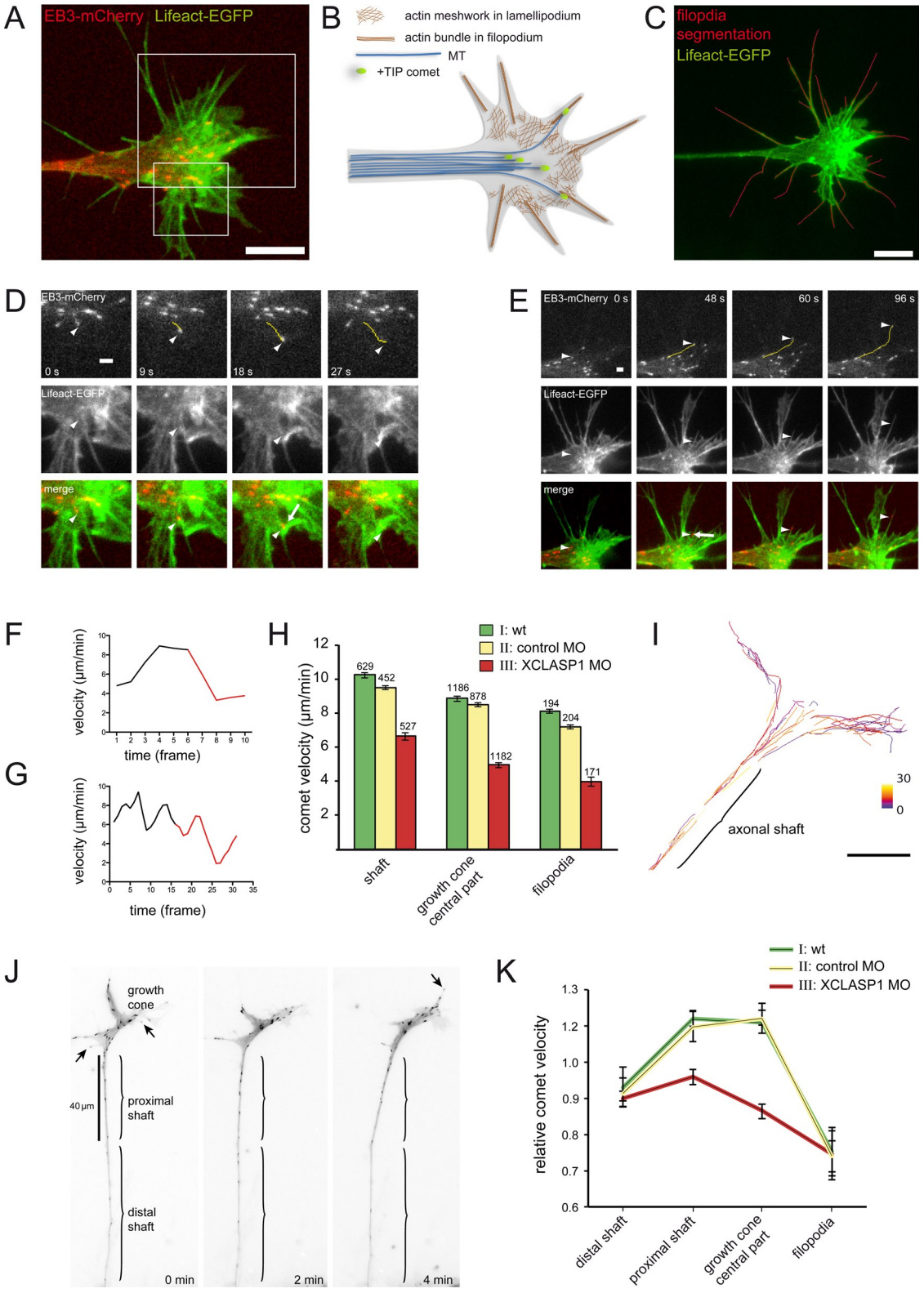

FIGURE 5: Advance rates of MT plus ends are reduced in the actin-rich leading edge of the growth cone. (A) *Xenopus* growth cone expressing EB3-mCherry (red) and Lifeact-EGFP (green) imaged at 3 s/frame. (B) Schematic view of localization of MTs, +TIPs (green), and actin in the growth cone. (C) Dynamic filopodia segmentation based on actin signal in A. (D) Detail (upper boxed region in A) of time lapse where an EB3 comet (position marked by arrowheads) advances toward the growth cone periphery and enters a region of high actin density. The yellow line marks the result of the automated tracking, and an arrow in the merged channel marks the initial contact between EB3-mCherry and actin. (E) Detail (lower boxed region in A) showing an EB3 comet (position marked by arrowheads) growing from the growth cone interior into a filopodium (entry point marked by arrow). (F, G) Velocity profiles of tracks in D and E,

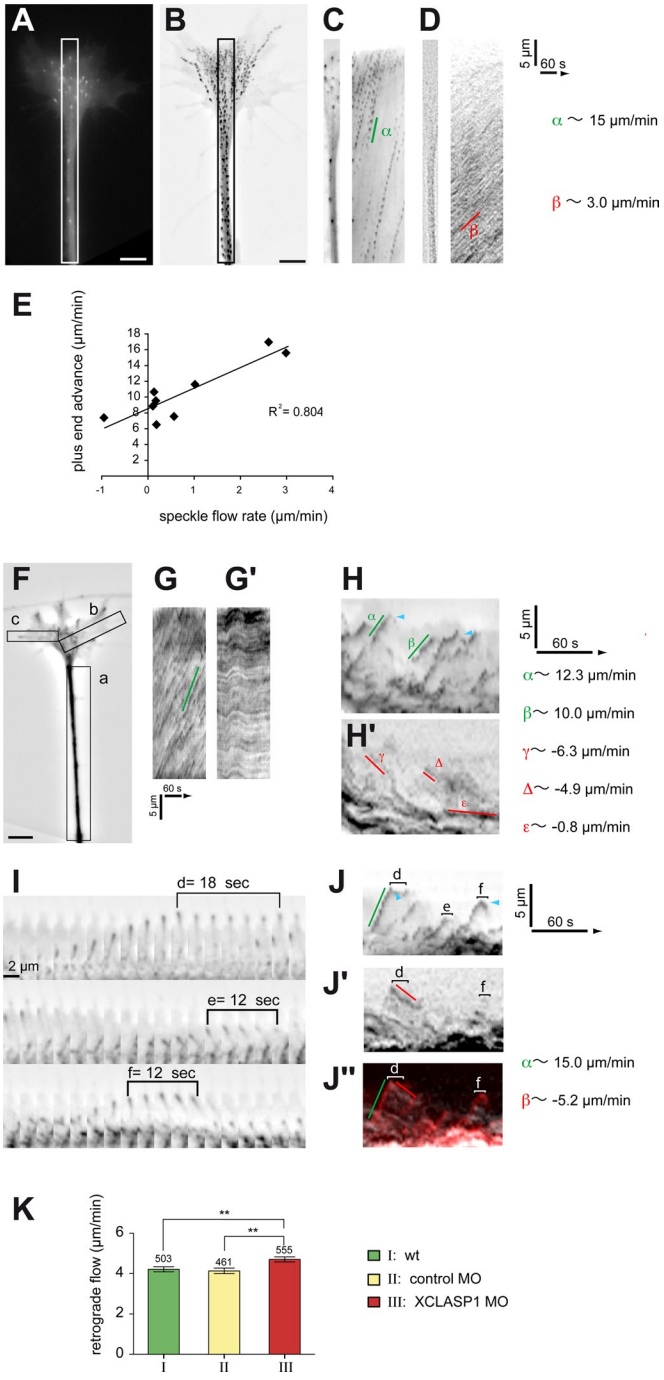

FIGURE 6: Microtubule growth is counteracted by retrograde flow at the leading edge. In spinal cord neurons, EB3-mCherry (A–C, F– J) was used for measurements of plus-end advance in combination with tubulin speckle microscopy to assess polymer movement (D, G′, H′). Fluorescence of EB3-mCherry and tubulin speckles is shown intensity inverted in all panels where the background is bright. (A) Plus-end labeling by EB3-mCherry in spinal cord neuron at start of time lapse. (B) Time-lapse sequence in maximum projection (39 frames, 190 s) shows straight EB3 tracks in shaft and curved tracks in the growth cone periphery. (C) Region of interest (see A) and kymograph, where the slope (α) of EB3-positive traces is a measure of plus-end advance rate. (D) Same region with kymograph of tubulin speckles. The angle (β) of speckle traces is a measure of the polymer bulk transport rate. (E). Linear correlation between tubulin bulk transport and plus-end advance rates in the axon shaft. Quantitation of rates as in C and D (10 axons). (F) Growth cone at beginning of time lapse with regions used for kymograph analysis. (G) Kymograph of shaft with EB3 positive plus ends; green line indicates slope (velocity) of moving plus ends. (G′) Kymograph of tubulin speckles that display lack of anterograde polymer transport. (H) Kymograph of region b, where EB3 traces indicate plus-end movement (green line), and "hooks" at the end of the traces near the growth cone periphery indicate plus-end stalling or retrograde transport (cyan arrowheads). (H′) Matching kymograph of tubulin speckles, which shows retrograde tubulin polymer transport of 5–6 µm/min. (I) Time lapse of detail of region c, where plus ends approach the growth cone margin and then stall while remaining positive for EB3. Phases of plus-end stalling at the periphery are indicated by brackets (d, e, and f). (J) Kymograph analysis of region c. EB3-positive plus ends first advance into the periphery and while still EB3 positive are transported backward, resulting in hooked traces (cyan arrowheads). (J′) Kymograph of tubulin speckles, which shows retrograde movement of speckles (red line), which can be attributed to MTs marked in I and J (d and f). (J″) Overlay of both kymographs; speckle movement–inverted gray scale, EB3-mCherry signal red. (K) Actin retrograde flow in the periphery of wild-type, control, and XCLASP1-depleted neurons. Number of traces analyzed is indicated. Error bars, SEM; $^{**}p < 0.01$. Scale bar where not labeled, 5 µm.

in XCLASP1 morpholino–injected neurons in comparison with controls (Figure 5, H and K). Of interest, our results on actin retrograde flow differ from the findings in HeLa cells, where CLASP1/2 depletion reduced retrograde flow by almost 50% (Mimori-Kiyosue *et al.*, 2005).

XCLASP1 promotes lamellipodial actin meshworks in growth cone veils

Spinal cord neurons in *Xenopus* are very heterogeneous in morphology (Tanaka and Kirschner, 1991), and we could not find strong differences in MT arrangement upon XCLASP1 depletion. However, when we investigated actin morphology, we found that with lowered XCLASP1 levels, an increased proportion of neurons showed scarce actin in the growth cone. In *Xenopus* neuronal growth cones, peripheral actin forms prominent filopodia, which extend rearward into the growth cone (intrapodia). Filopodia are interconnected by lamellipodial veils, which show a dense meshwork a few micrometers into the growth cone (Strasser *et al.*, 2004; Korobova and Svitkina, 2008; Figure 7, A and B). The prevalence of growth cones that lack cortical meshwork and filopodia anchorage (Figure 7C) was around 20% in control and uninjected neurons but much higher in XCLASP1-depleted spinal cord cultures (Figure 7D, compare III with I and II). These growth cones showed inward bending of veils

respectively. The time points where contact with actin occurs (arrows in D and E) are indicated by a change in color. (H) Mean velocities of EB3 comets in the shaft, the growth cone central part, and filopodia for uninjected (wt) vs. morpholino-injected ones. The number of analyzed tracks is indicated. (I) Color visualization of the mean velocities of automatically tracked MTs over 195 s (3 s/frame); see Supplemental Movie S5. Color code extends from 0 to 30 µm/min. (J) EB3 imaging in proximal and distal shaft; arrows mark EB3 comets in filopodia. (K) Quantitation of comet velocity in neurons imaged as shown in J. Average instantaneous velocities are normalized to the median value in distal shaft for each treatment. Scale bars, 10 µm (A, C, I), 2 µm (D, E).

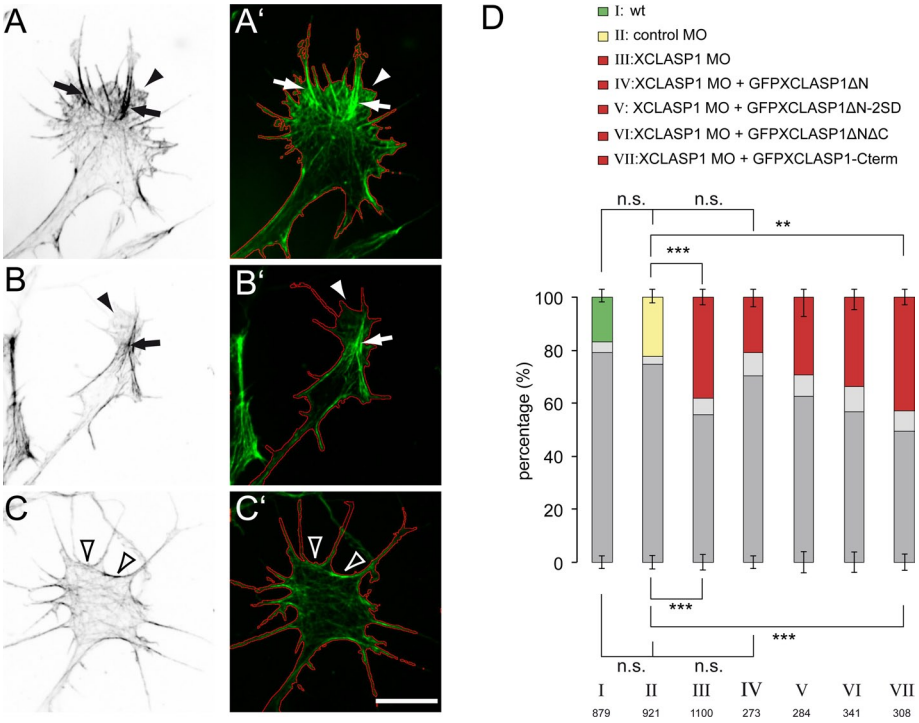

FIGURE 7: XCLASP1 promotes lamellipodial actin architecture. Classification of F-actin morphology in fixed growth cones. Staining of F-actin imaged by confocal microscopy is shown intensity inverted (A–C) or in green (A′–C′); the growth cone outline is highlighted in red (A′–C′). (A) Well-spread growth cone with many filopodia, where actin bundles extend into the interior of the growth cone (arrows). Lamellipodia bulge out as convex protrusions (arrowheads) between filopodia. (B, B′) A strongly polarized growth cone with strong actin bundles (arrows) and a big lamellipodium (arrowhead). (C, C′) Growth cone devoid of lamellipodia; the membrane between filopodia is predominantly concave (open arrowheads), and no strong actin bundles are found inside the growth cone. Images in A, B, and C were taken from wt, control MO–injected neurons, and XCLASP1-MO–injected neurons, respectively. (D) Classification of actin morphology. Proportion of growth cones with strong actin fibers in the interior and/or lamellipodial actin networks as in A and B (dark gray) vs. proportion of growth cones lacking lamellipodia and strong actin bundles in the growth cone as in C (colored according to morpholino). Light gray represents growth cones that fit neither category. Experiments were as follows: I, $n = 20$, II; $n = 25$; III, $n = 20$; IV, $n = 3$; V, $n = 6$, VI; $n = 4$, VII, $n = 4$. Numbers of cells analyzed per treatment are indicated. Values in wild-type neurons (I) were significantly different from those for all other treatments except where indicated (n.s.). Error bars, SEM; ***$p < 0.0001$, **$p < 0.01$.

between filopodia (Figure 7C, empty arrowheads), whereas growth cones with pronounced actin meshwork in the growth cone interior showed convex veils (Figure 7, A and B, arrowheads). The increased incidence of growth cones with concave veils and lack of peripheral actin meshwork (Figure 7D, color, compare III with I and II) in XCLASP1-depleted neurons compared with wild type and control morpholino suggests that XCLASP1 is important for these structures. This suggested that XCLASP1 promotes formation or maintenance of lamellipodia. Indeed coinjection of a morpholino-resistant XCLASP1ΔN fragment fused to EGFP rescued the proportion of growth cones with an actin distribution as shown in Figure 7C to control levels (Figure 7D, IV).

On the basis of our finding that XCLASP1 is important for MT dynamics, we sought to investigate whether the MT-binding domains in XCLASP1 are important for actin morphology. We constructed a series of XCLASP1 truncations (Figure 8A) and a construct identical to XCLASP1ΔN with two point mutations (XCLASP1ΔN-2SD; Figure 8B) near the only SXIP motif of XCLASP1 (Kumar *et al.*, 2012). EGFP-XCLASP1ΔN-2SD showed reduced MT plus-end binding (Figure 8C and Supplemental Figure S1, C–F). EGFP-XCLASP1ΔN-2SD failed to efficiently rescue the actin phenotype (Figure 7D, compare IV and V). In addition, the C-terminus of XCLASP1 (XCLASP1-Cterm), responsible for interaction with CLIP-170 (Akhmanova *et al.*, 2001; Figure 8A), showed no rescue of the actin phenotype. This construct only showed cytoplasmic localization in growth cones and binding to the microtubule-organizing center in the cell body (Figure 8C, last two panels). The middle part of XCLASP1, XCLASP1ΔNΔC, showed incomplete rescue. We cannot conclude about the contribution of the C-terminus to actin integrity, as the rescue was not significantly different from either XCLASP1 morpholino (III) or control MO (II). In summary, our data suggest that the capacity of XCLASP1 to associate with plus ends through the SXIP domain is essential for convex lamellipodia and intrapodia.

A previous electron microscopy study of protruding and retracting actin veils in *Xenopus* neurons highlighted that protrusion was always associated with a dense actin meshwork behind the membrane and retraction with scarce actin, often forming parallel bundles to the membrane (Mongiu *et al.*, 2007). To analyze the fine structure of actin, we used structured illumination microscopy (SIM). In growth cones typical for control and wild-type neurons, we could clearly identify filopodia, which were embedded as actin bundles in lamellipodia (intrapodia; Figure 9, A′ and B′, arrows in insets), and thinner actin filaments with varying angles that are typical for lamellipodia (Figure 9, A′ and B′, arrowheads in insets; Korobova and Svitkina, 2008). In contrast, the growth cone periphery in XCLASP1-depleted neurons lacked dense actin meshwork (Figure 9, C–D′), only a few actin bundles were visible, and they were associated with neither intrapodia nor lamellipodia. The membrane between filopodia was concave and resembled very much the rear-oriented veils of other growth cones (Figure 9B′, open arrowhead). In summary, XCLASP1-depleted neurons had an increased number of growth cones that show an actin distribution in veils reminiscent of retracting rather than protruding periphery as described by Mongiu *et al.* (2007). This hints to disturbed lamellipodial protrusion in XCLASP1-depleted neurons. We also analyzed XCLASP1-depleted neurons by live imaging using Lifeact-GFP. The resolution of actin in these images is far inferior to that in fixed samples; however XCLASP1-depleted growth cones show reduced lamellipodial activity compared with controls (see Supplemental Movies S7–S9).

DISCUSSION

Automated tracking of MTs reveals differential regulation of MT advance in shaft, growth cone, and filopodia

We devised a method of analyzing MT dynamics in neurons. On the basis of low expression levels of the +TIP EB3 to track plus ends

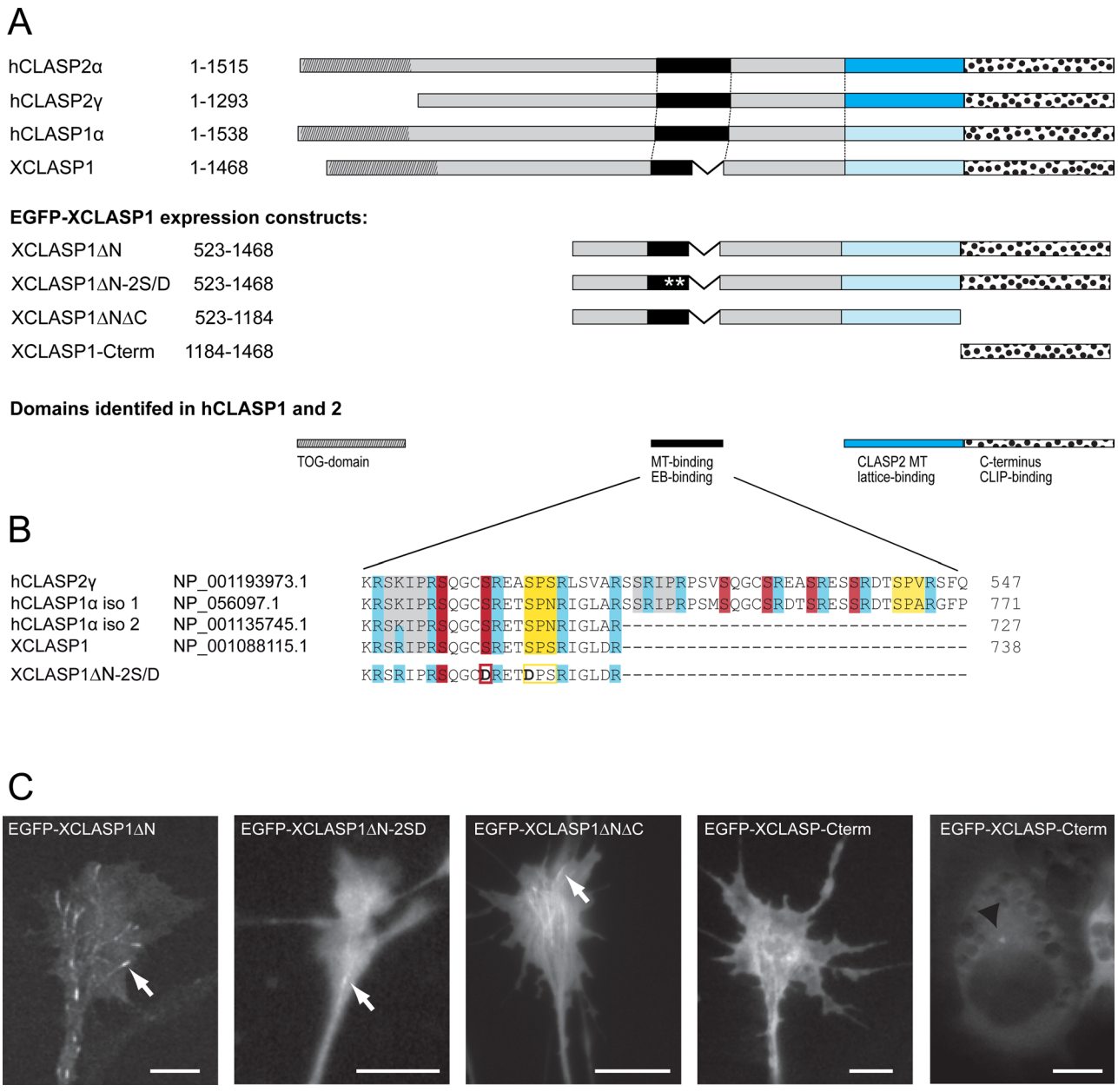

FIGURE 8: XCLASP1 domains and localization of XCLASP1 truncations. (A) Schematic representation of human CLASP1 and 2 and the shorter isoform CLASP2γ. TOG domains are present in CLASP1 and 2; XCLASP1 possesses an N-terminal TOG domain (Patel *et al.*, 2012). The central minimal domain for MT association and the lattice binding were identified in hCLASP2 (Mimori-Kiyosue *et al.*, 2005; Kumar *et al.*, 2009). (B) Alignment of SXIP motives in human CLASP1 (NP_056097), CLASP2 (NP_055012), and XCLASP1 (NP_001088115), adapted from Kumar *et al.* (2012). Note that XCLASP1 possesses only one SXIP motif, as do certain isoforms of hCLASP1. SXIP motif-associated arginines (blue), GSK-3 (red), and CDK (yellow) phosphorylation sites are conserved. The mutations in XCLASP1ΔN-S2/D (highlighted in bold) are on serines close to the SXIP domain and predicted to help in EB binding (Buey *et al.*, 2012). Serine-to-glutamate exchanges at positions S726 and S730 were designed as phosphomimetics of GSK-3 and CDK phosphorylation, respectively. (C) Expression of XCLASP1 truncations as EGFP fusion proteins. Binding to MTs in the growth cone is indicated by white arrows; binding to the microtubule-organizing center in the neuronal cell body is indicated by a black arrowhead.

(Stepanova *et al.*, 2003, 2010) and wide-field fluorescence time-lapse microscopy, we developed automated tracking to determine the velocity, track length, and lifetime of MT tracks. Our algorithm can operate on sequences acquired at low frame rates to minimize the exposure of the cells, which is extremely important for neurons, as they are very sensitive to phototoxicity.

For the first time, we can compare MT dynamics in different compartments of the vertebrate axon (Figure 5). Previously, MTs growing along the axonal shaft were shown to progress without being influenced by their position (e.g., branch point; Stepanova *et al.*, 2010). In *Xenopus* spinal cord neurons used here, plus-end velocities depend on location: MT advance is highest in the axon shaft close to

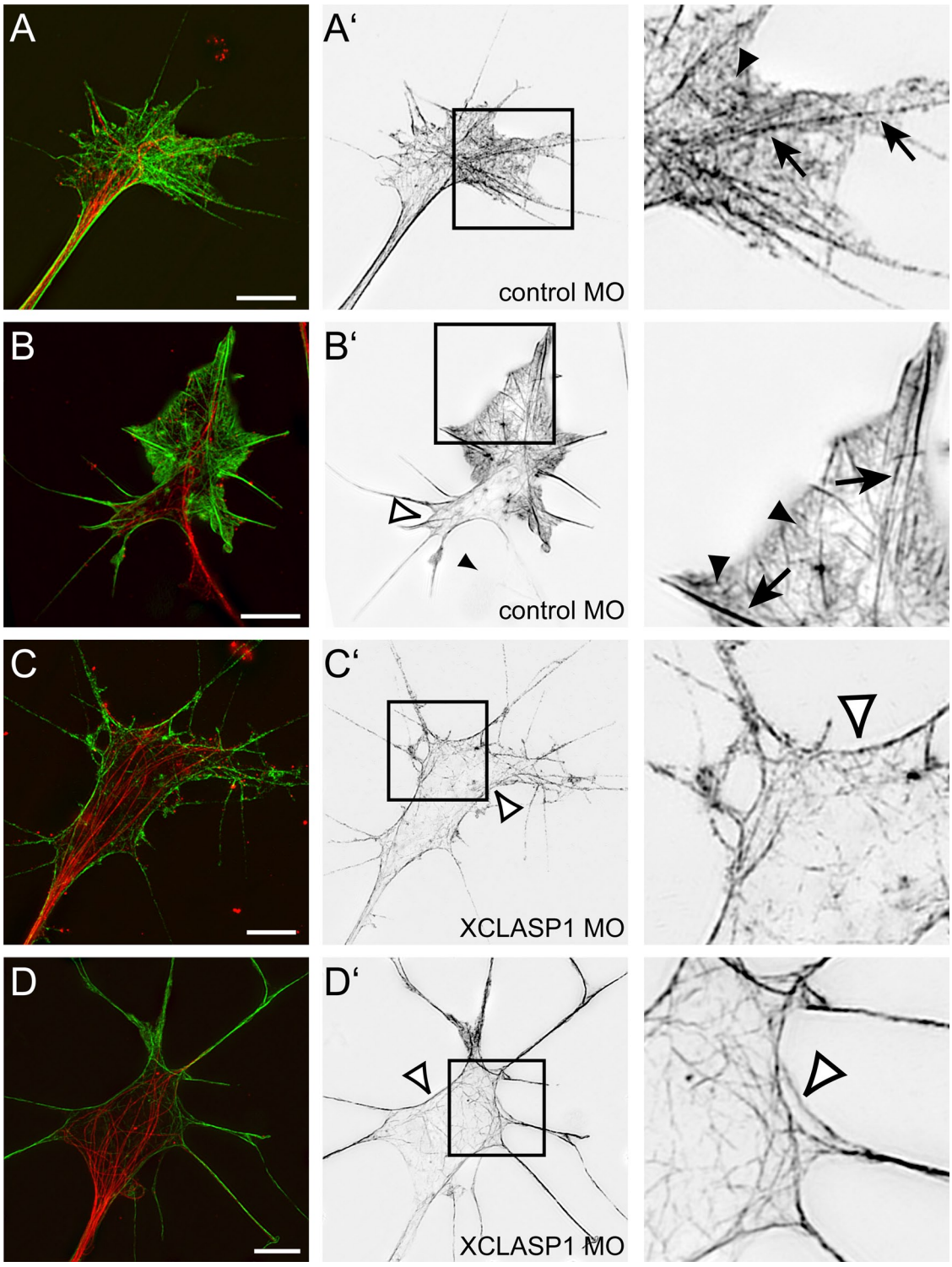

FIGURE 9: Actin morphology is altered in XCLASP1-depleted growth cones. SIM of *Xenopus* growth cones, where F-actin stained by phalloidin is shown in green and MTs in red (A–C). For clarity phalloidin staining is shown intensity inverted (A′–D′ and insets). (A–B′) Examples of actin morphology that are characteristic for most growth cones in wild-type or control MO–injected neurons. Filopodia are anchored in the growth cone with actin bundles that are anchored deep inside the growth cone (arrows). These prominent actin bundles are embedded in a dense lamellipodial actin meshwork (arrowheads). (C–D′) In XCLASP1-depleted growth cones (XCLASP1 MO) filopodia do not extend rearward into the growth cone interior and lamellipodia are missing. Instead, the outline between filopodia is bent inward (open arrowheads). Scale bar, 5 μm; insert size, 10 × 10 μm.

the growth cone (Figure 5K) and decreases as MT ends reach the growth cone periphery (Figure 5, H and K). These differences are reminiscent of the graded MT dynamics in epithelial cells, which help MTs to explore the periphery (Komarova *et al.*, 2002). The periphery of U2OS cells in wound healing also showed reduced MT advance rates compared with the cell interior (Nishimura *et al.*, 2012).

XCLASP1 promotes microtubule advance in the growth cones but not in the shaft

Dynamic MTs in neuronal growth cones are necessary for directed outgrowth (Sabry *et al.*, 1991; Tanaka and Kirschner, 1991; Tanaka *et al.*, 1995; Tanaka and Kirschner, 1995; Dent and Kalil, 2001; Zhou and Cohan, 2004). Stabilization of MTs by Taxol is sufficient to induce growth cone turning (Buck and Zheng, 2002), and MT-stabilizing proteins like MAP1B have been shown to influence guidance (Mack *et al.*, 2000; Hahn *et al.*, 2005). Many +TIPs show high expression in the developing nervous system and especially in outgrowing nerves (Park *et al.*, 2012). Indeed we found that XCLASP1 mRNA localization in spinal cord nerves was high during axon outgrowth but disappeared in later stages (Figure 1, A–C). In a genetic screen in *Drosophila*, we previously identified the CLASP homologue Orbit (Lee *et al.*, 2004) downstream of Slit repulsion. With a loss-of-function approach, we depleted XCLASP1 and found that MT advance in the growth cone is reduced (Figure 4 and Table 1). Of interest, XCLASP1 regulated MT dynamics only in the growth cone and the most proximal shaft. In a segment >40 µm away from the growth cone, XCLASP1 depletion showed no effect on comet velocities.

A study by Hur *et al.* (2011) proposed a dual role for CLASPs in axon outgrowth. In cortical neurons where GSK-3 activity is low, MT binding of CLASP2 through its lattice binding (Kumar *et al.*, 2009) inhibited outgrowth. In contrast, depletion of CLASP1 and 2 in dorsal root ganglia led to decreased outgrowth, pointing to a role of CLASPs in axon elongation (Hur *et al.*, 2011). This latter effect is consistent with our results on XCLASP1 in outgrowing *Xenopus* spinal cord neurons.

Reduced MT advance in the growth cone correlates with dampened axon extension

Several studies pharmacologically interfered with pioneer MTs and found a link between MT dynamics and axon behavior. In cortical neurons, both Taxol (10 nM) and nocodazole (33 nM) reduced axon extension and led to curved axon trajectories (Dent and Kalil, 2001). Using automated tracking, we were able to quantify the effects of Taxol on plus-end advance. Taxol at <10 nM reduced plus-end velocities in the growth cone while still allowing for polymerization, as indicated by EB3-positive comets (Figure 3, C and D, and Supplemental Movie 3). Low Taxol concentrations and XCLASP1 depletion resulted in subtle interference with +TIP advance (Figure 4D), and both interfered with axon extension and directionality (Figure 1, E–H). Microtubule drugs applied in a bath application necessarily affect the whole axon. However, XCLASP depletion affected dynamics only in and near the growth cone, suggesting that it is the changed MT dynamics in the growth cone that affects axon outgrowth.

Mechanistically it is hard to conceive how axon elongation and MT advance into the periphery of the growth cone might be linked directly, for example, by MTs pushing the growth cone forward, as axon elongation is on average 10 times lower than MT polymerization (Lee *et al.*, 2004). An attractive model is that dynamic MTs deliver signaling factors that influence actin polymerization, retrograde flow, or substrate coupling (Suter *et al.*, 2004). This is also compatible with cell type–specific effects of altered pioneer MT dynamics. For example, Taxol at the same concentrations as used here promoted outgrowth in regenerating sensory neurons in vivo (Hellal *et al.*, 2011).

MTs at the leading edge are affected by actin-mediated retrograde flow

Neuronal growth cones are very dynamic, and although advance rates depend on the substrate (Lee *et al.*, 2004; Jacques-Fricke *et al.*, 2006), 2 µm/min is common for *Xenopus* spinal cord neurons plated on laminin (Tanaka *et al.*, 1995). Tubulin speckle microscopy demonstrated forward transport of MT polymer in the shaft and central domain at rates up to 3 µm/min (Figure 6), consistent with earlier measurements in *Xenopus* neurons, where forward transport was attributed to pulling tension generated by the growth cone (Chang *et al.*, 1998). We found that in the shaft there is a clear correlation between MT bulk transport and plus-end advance, where anterograde transport positively affects plus-end translocation (Figure 6E).

In contrast to the shaft, MTs in the growth cone periphery are transported backward (Figure 6, H–J″), and the rates at which they are transported are similar to retrograde flow rates of actin (Figure 6K). We observed MTs at the cortex that seemingly paused but were actually in a tug of war between polymerization and retrograde movement of the tubulin polymer (Figure 6, H–J). This suggests that in vertebrate growth cones MT retrograde transport cooperates with catastrophe in removing MTs from the periphery, very much like what was demonstrated for invertebrate neurons (Medeiros *et al.*, 2006; Burnette *et al.*, 2007).

XCLASP1 is necessary to maintain protrusive actin morphology

CLASPs have a role as rescue factors that mediate rapid transition from depolymerization to polymerization (Al-Bassam and Chang, 2011), but in mammalian cells CLASPs seems to promote not only rescue but also catastrophe to keep plus ends near to the periphery (Mimori-Kiyosue *et al.*, 2005). Similarly, CLASP was shown to maintain the MT array at the cortex of *Drosophila* cells, but by keeping MTs in a paused state (Sousa *et al.*, 2007). In accordance with these observations, we found that XCLASP1 is important for maintaining pioneer MTs in the growth cone periphery. Our data suggest that transitions from the growing state in XCLASP1-depleted growth cones are not altered, since track lifetimes are even slightly increased (Figure 4C). However, we are limited in our analysis because we cannot discriminate between transitions to catastrophe and pause, nor can we identify rescue events. The reduced plus-end velocities we measured do not necessarily signify reduced polymerization, because MTs are subject to considerable translocation movements (Figure 6). To disentangle these processes in the XCLASP1-depleted neuron, automated quantitative speckle microscopy would be required in addition to plus-end tracking.

Previously, CLASPs were shown to affect retrograde flow (Mimori-Kiyosue *et al.*, 2005). Because retrograde flow would also change pioneer MT advance, we looked at actin in XCLASP1-depleted neurons. We found that retrograde flow was hardly changed (Figure 6K) but were intrigued that actin architecture in the growth cone periphery changed when XCLASP1 was depleted. Our morphological analysis indicates that XCLASP1 promotes lamellipodial actin meshwork in growth cone veils. A significant number of XCLASP1-depleted growth cones show concave veils poor in actin filaments (Figure 9C′ and inset), and our high-resolution images with SIM closely resemble electron micrographs of retracting actin veils (Mongiu *et al.*, 2007). In addition, live imaging supports the interpretation that XCLASP1 function is necessary for lamellipodial protrusion (Supplemental Movie S9).

It is unclear whether XCLASP1 is important for formation or maintenance of lamellipodial networks, and we can only speculate on the mechanism. XCLASP1 might bind actin indirectly, such as through cross-linker short stop (Rogers *et al.*, 2004), and it has also been reported to bind actin filaments directly (Tsvetkov and Popov, 2007). The actin morphology in XCLASP1-depleted neurons resembles to a certain degree the phenotype in rac-inhibited *Xenopus*

neurons (Rajnicek *et al.*, 2006), which might suggest that pioneer MTs are important to deliver signaling molecules. Indeed, we showed that the capacity XCLASP1 to bind to MT plus ends is important for actin architecture. We could compensate for the effect of the XCLASP1 morpholino by concomitant expression of GFPXCLASP1ΔN but not by a mutated form that displayed reduced plus-end binding. This suggests that XCLASP1 plays a role in coordination of actin and microtubules in growth cone protrusion.

MATERIALS AND METHODS

Constructs

Murine EB3-2FLAGi-mCherry (Straube and Merdes, 2007) was cloned into pCS2 vector to result in EB3-mCherry pCS2 or EB3-EGFP pCS2. Similarly, Lifeact-EGFP was cloned into pCS2 for in vitro transcription of capped mRNA with an SP6 polymerase. *Xenopus* CLASP 1 cDNA (National Center for Biotechnology Information gene ID 494817) was obtained in pCMV-Sport6 from Source BioScience (Nottingham, United Kingdom) and used as a template for the design of morpholino oligonucleotides and in situ probes. An N-terminal deletion of XCLASP1 comprising amino acids 524–1468 (XCLASP1ΔN) was inserted into pCS2-EGFP, and point mutations in S726 and S730 to glutamate resulted in XCLASP1ΔN-S2/D. Truncations XCLASP1ΔNΔC and XCLASP1-Cterm were inserted in pCS2-EGFP for in vitro mRNA synthesis and are described in Figure 8.

Injection in *X. laevis* embryos

Fertilized eggs of *X. laevis* were injected at the four-cell stage into dorsal blastomeres with 5 nl of solution in vitro–transcribed capped mRNA (mMessage mMachine, Ambion, Austin, TX) at different concentrations (0.019 μg/μl EB3-EGFP, 0.028 μg/μl EB3-mCherry, 0.06 μg/μl Lifeact-EGFP, 0.1 μg/μl EGFP tubulin). For speckle microscopy HiLyte488 porcine tubulin (Cytoskeleton, Denver, CO) was injected together with mRNA at concentration of 0.2–1 μg/ml. EGFP-XCLASP1ΔN, EGFP-XCLASP1ΔNΔC, and EGFP-XCLASP1-Cterm mRNA were injected at 0.15, 0.1, and 0.7 μg/ml, respectively. At stage 28, embryos were dissected as described (Tanaka and Kirschner, 1991). Pieces of spinal cord were plated on glass-bottom dishes coated with laminin (20 μg/ml; Sigma-Aldrich, St. Louis, MO) in culture medium (Ming *et al.*, 1997) supplemented with 100 ng/ml brain-derived neurotrophic factor (Sigma-Aldrich). Outgrowing neurons were imaged or fixed for immunocytochemistry 14–18 h after plating. Taxol (Sigma-Aldrich) was added in conditioned medium in concentrations indicated 1 h before imaging.

For knockdown experiments 0.4 pmol of XCLASP1 morpholino 5′-ATGGAACAGGGAATGGACTACTGGC-3′ or control morpholino 5′-CCTCTTACCTCAGTTACAATTTATA-3′ (Gene Tools, Philomath, OR) was injected at the four-cell stage together with mRNA or 1.5 μg/μl fixable fluorescent dextran (Invitrogen, Carlsbad, CA).

Time-lapse microscopy

Image sequences for automated tracking were recorded on an inverted Nikon TiE microscope equipped with a 60 or 100×/numerical aperture (NA) 1.4 Planapo VC objective and a Nikon Intensilight (Nikon, Melville, NY) as light source with a frame rate of 3 s/frame. Cameras used were either the charged-coupled device (CCD) ORCA (Hamamatsu, Hamamatsu, Japan) or the Xion DU-897 electron multiplier CCD (Andor, Belfast, United Kingdom), resulting in a pixel size of 107 or 160 nm, respectively. For EB3 tracking in distal and proximal shaft, an sNEO cMOS (Andor) was used in combination with a 60×/NA 1.4 objective, resulting in a field of view of 200 × 270 μm and a pixel size of 108 nm.

For analysis of axon outgrowth and the collapse assay, bright-field images were recorded with 3-min intervals for 30 min using a Nikon 20×/NA 0.75 Planfluor objective. Injected neurons were identified by EGFP fluorescence recorded at the beginning and end of the sequence. The path of the growth cone was tracked manually.

Automated +TIP tracking and statistical analysis

We developed a probabilistic approach for tracking EB3 comets in fluorescence microscopy image sequences. In our approach, each EB3 comet is represented via a 2D anisotropic Gaussian function that is parameterized by the position of the comet (x, y), its peak intensity I_{max}, and the standard deviations σx and σy. We assumed that the orientation of the comet agrees with the orientation of its velocity vector (x', y'). At each time point, our approach carries out two steps: 1) detection and localization of comets, and 2) estimation of the position of the individual comets. To detect and localize comets, we first used a Gaussian filter to reduce the image noise. The values for the SD σF of the filter were set based on the size of the comets (typically, we used a value of $\sigma F = 3$). To suppress the background, intensity values below a threshold T_{clip} were removed. The clipping threshold T_{clip} was computed as the mean intensity of the image plus a factor c times the SD of the image intensities. Image regions corresponding to EB3 comets were detected by performing a search for local intensity maxima. To localize comets, we fitted a 2D Gaussian function to each candidate image region.

To estimate the position of the tracked comets, we predicted the position of each comet using a Kalman filter with a constant-velocity motion model. Initial estimates for the velocity components were obtained by computing the optical flow between two consecutive images. To find the correspondences between the positions predicted by the Kalman filter and the positions computed by the 2D Gaussian fitting scheme, we used a global nearest-neighbor approach (Sbalzarini and Koumoutsakos, 2005). Using the predicted position, as well as the position from 2D Gaussian fitting, the Kalman filter calculated the final position estimate for each comet.

Track data were saved as text files and visualized by a custom-designed track visualization plug-in for ImageJ (National Institutes of Health, Bethesda, MD; Abramoff *et al.*, 2004). This allowed tracks to be sorted, exported, and viewed as overlays on top of the corresponding image sequences. Tracks with durations shorter than three frames (15 s) were discarded. Kymograph analysis of EB3 comets was performed by drawing manually segmented lines defining the image track and creating kymographs with the ImageJ plug-in bundle Multiple Kymograph by J. Rietdorf and A. Seitz (European Molecular Biology Laboratory, Heidelberg, Germany).

Statistical analysis and graphs were made using Prism 5 (GraphPad Software, La Jolla, CA). Mann–Whitney tests were used to test for statistical significance in data of non-Gaussian distributions.

Dynamic segmentation of filopodia

For segmentation of the filopodia, first, thin structures in the original actin image were enhanced based on a method previously used to detect blood vessels (Frangi *et al.*, 1998). To detect image regions corresponding to thin structures, we then applied an automatic thresholding technique (Zack *et al.*, 1977) to the enhanced image. With this technique, also known as the triangle method, the histogram is normalized, and then the line between the maximum and minimum value of the histogram is determined. Afterward, the distances between this line and all values of the histogram are computed, and the intensity value for which the distance is maximal is taken as the threshold.

To exclude those regions that corresponded to the inner part of the growth cone, we segmented the central part of the growth cone and excluded it from the segmentation result for filopodia. For segmentation of the central part of the growth cone, we applied Otsu's method (Otsu, 1979), as well as morphological operations (opening and closing). The method of Otsu subdivides an image into pixels of two classes so that their intraclass variance is minimal. To determine moving comets along filopodia, we considered only those parts of a trajectory from tracked comets that are located within the segmented filopodia and used this information to subdivide tracks for analysis.

Analysis of tubulin speckles

Using ImageJ, we enhanced time-lapse sequences with tubulin speckles by a difference-of-Gaussians method in which the image was first smoothed by a small Gaussian filter to reduce noise ($\sigma F_1 = 1$), and a more highly filtered duplicate of the image ($\sigma F_2 = 4$) was then subtracted. The resulting difference image showed the particles more clearly. To analyze flow, rectangular regions of interest were cropped and the dimensions of the image reordered to convert an *x*–*y*–time stack into an *x*–time–*y* stack. A kymograph was then created using a maximum projection along the *y*-axis. By manually identifying the angles of speckle traces, we calculated their velocities along the *x*-axis. Additional methods are described in the Supplemental Data.

ACKNOWLEDGMENTS

We thank Rebecca Heald for Xorbit antibody, Michael Sixt for Lifeact-EGFP, and Anne Straube for EB3-mCherry constructs. We thank Lars Kaderali for advice in statistics. We are extremely grateful to Christoph Niehr's lab and especially to Ya-Lin Huang for access to frogs and Doris Wedlich for providing XLKE cells. We are grateful to Nikon GmbH for continued support of the Nikon Imaging Center at the University of Heidelberg. A.M. was supported by the Exzellenzcluster CellNetworks Heidelberg and P.B. by Heidelberg Molecular Life Science. K.R. gratefully acknowledges support of the Bundesministerium für Bildung und Forschung project ViroQuant FORSYS, Research Units for Systems Biology.

REFERENCES

Abramoff MD, Magalhaes PJ, Ram SJ (2004). Image processing with ImageJ. Biophotonics Int 11, 36–42.

Akhmanova A *et al.* (2001). Clasps are CLIP-115 and -170 associating proteins involved in the regional regulation of microtubule dynamics in motile fibroblasts. Cell 104, 923–935.

Akhmanova A, Steinmetz MO (2008). Tracking the ends: a dynamic protein network controls the fate of microtubule tips. Nat Rev Mol Cell Biol 9, 309–322.

Al-Bassam J, Chang F (2011). Regulation of microtubule dynamics by TOG-domain proteins XMAP215/Dis1 and CLASP. Trends Cell Biol 21, 604–614.

Applegate KT, Besson S, Matov A, Bagonis MH, Jaqaman K, Danuser G (2011). plusTipTracker: quantitative image analysis software for the measurement of microtubule dynamics. J Struct Biol 176, 168–184.

Buck KB, Zheng JQ (2002). Growth cone turning induced by direct local modification of microtubule dynamics. J Neurosci 22, 9358–9367.

Buey RM *et al.* (2012). Sequence determinants of a microtubule tip localization signal (MtLS). J Biol Chem 287, 28227–28242.

Burnette DT, Schaefer AW, Ji L, Danuser G, Forscher P (2007). Filopodial actin bundles are not necessary for microtubule advance into the peripheral domain of *Aplysia* neuronal growth cones. Nat Cell Biol 9, 1360–1369.

Chang S, Rodionov VI, Borisy GG, Popov SV (1998). Transport and turnover of microtubules in frog neurons depend on the pattern of axonal growth. J Neurosci 18, 821–829.

Chang S, Svitkina TM, Borisy GG, Popov SV (1999). Speckle microscopic evaluation of microtubule transport in growing nerve processes. Nat Cell Biol 1, 399–403.

Dent EW, Gertler FB (2003). Cytoskeletal dynamics and transport in growth cone motility and axon guidance. Neuron 40, 209–227.

Dent EW, Kalil K (2001). Axon branching requires interactions between dynamic microtubules and actin filaments. J Neurosci 21, 9757–9769.

Frangi AF, Niessen WJ, Vincken KL, Viergever MA (1998). Multiscale vessel enhancement filtering. In: Medical Image Computing and Computer-Assisted Intervention (MICCAI), ed: WM Wells, ACF Colchester, and SL Delp, Heidelberg, Germany: Springer, 130–137.

Godinez WJ, Lampe M, Wörz S, Müller B, Eils R, Rohr K (2009). Deterministic and probabilistic approaches for tracking virus particles in time-lapse fluorescence microscopy image sequences. Med Image Anal 13, 325–342.

Hahn CM, Kleinholz H, Koester MP, Grieser S, Thelen K, Pollerberg GE (2005). Role of cyclin-dependent kinase 5 and its activator P35 in local axon and growth cone stabilization. Neurosci 134, 449–465.

Hannak E, Heald R (2006). Xorbit/CLASP links dynamic microtubules to chromosomes in the *Xenopus* meiotic spindle. J Cell Biol 172, 19–25.

Hellal F *et al.* (2011). Microtubule stabilization reduces scarring and causes axon regeneration after spinal cord injury. Science 331, 928–931.

Hur EM, Saijilafu Lee BD, Kim SJ, Xu WL, Zhou FQ (2011). GSK3 controls axon growth via CLASP-mediated regulation of growth cone microtubules. Genes Dev 25, 1968–1981.

Inoue YH, do Carmo Avides M, Shiraki M, Deak P, Yamaguchi M, Nishimoto Y, Matsukage A, Glover DM (2000). Orbit, a novel microtubule-associated protein essential for mitosis in *Drosophila melanogaster*. J Cell Biol 149, 153–166.

Jacques-Fricke BT, Seow Y, Gottlieb PA, Sachs F, Gomez TM (2006). Ca^{2+} influx through mechanosensitive channels inhibits neurite outgrowth in opposition to other influx pathways and release from intracellular stores. J Neurosci 26, 5656–5664.

Komarova YA, Vorobjev IA, Borisy GG (2002). Life cycle of MTs: persistent growth in the cell interior, asymmetric transition frequencies and effects of the cell boundary. J Cell Sci 115, 3527–3539.

Korobova F, Svitkina T (2008). Arp2/3 complex is important for filopodia formation, growth cone motility, and neuritogenesis in neuronal cells. Mol Biol Cell 19, 1561–1574.

Kumar P, Chimenti MS, Pemble H, Schonichen A, Thompson O, Jacobson MP, Wittmann T (2012). Multisite phosphorylation disrupts arginine-glutamate salt bridge networks required for binding of cytoplasmic linker-associated protein 2 (CLASP2) to end-binding protein 1 (EB1). J Biol Chem 287, 17050–17064.

Kumar P, Lyle KS, Gierke S, Matov A, Danuser G, Wittmann T (2009). GSK-3beta phosphorylation modulates CLASP-microtubule association and lamella microtubule attachment. J Cell Biol 184, 895–908.

Lansbergen G *et al.* (2006). CLASPs attach microtubule plus ends to the cell cortex through a complex with LL5beta. Dev Cell 11, 21–32.

Lee H, Engel U, Rusch J, Scherrer S, Sheard K, Van Vactor D (2004). The microtubule plus end tracking protein Orbit/MAST/CLASP acts downstream of the tyrosine kinase Abl in mediating axon guidance. Neuron 42, 913–926.

Lee H, Van Vactor D (2003). Neurons take shape. Curr Biol 13, R152–R161.

Lemos CL, Sampaio P, Maiato H, Costa M, Omel'yanchuk LV, Liberal V, Sunkel CE (2000). Mast, a conserved microtubule-associated protein required for bipolar mitotic spindle organization. EMBO J 19, 3668–3682.

Ma Y, Shakiryanova D, Vardya I, Popov SV (2004). Quantitative analysis of microtubule transport in growing nerve processes. Curr Biol 14, 725–730.

Mack TG, Koester MP, Pollerberg GE (2000). The microtubule-associated protein MAP1B is involved in local stabilization of turning growth cones. Mol Cell Neurosci 15, 51–65.

Matov A, Applegate K, Kumar P, Thoma C, Krek W, Danuser G, Wittmann T (2010). Analysis of microtubule dynamic instability using a plus-end growth marker. Nat Methods 7, 761–768.

Medeiros NA, Burnette DT, Forscher P (2006). Myosin II functions in actin-bundle turnover in neuronal growth cones. Nat Cell Biol 8, 215–226.

Mimori-Kiyosue Y *et al.* (2005). CLASP1 and CLASP2 bind to EB1 and regulate microtubule plus-end dynamics at the cell cortex. J Cell Biol 168, 141–153.

Mimori-Kiyosue Y, Shiina N, Tsukita S (2000). The dynamic behavior of the APC-binding protein EB1 on the distal ends of microtubules. Curr Biol 10, 865–868.

Ming GL, Song HJ, Berninger B, Holt CE, Tessier-Lavigne M, Poo MM (1997). cAMP-dependent growth cone guidance by netrin-1. Neuron 19, 1225–1235.

Mitchison T, Kirschner M (1984). Dynamic instability of microtubule growth. Nature 312, 237–242.

Mongiu AK, Weitzke EL, Chaga OY, Borisy GG (2007). Kinetic-structural analysis of neuronal growth cone veil motility. J Cell Sci 120, 1113–1125.
Morrison EE (2007). Action and interactions at microtubule ends. Cell Mol Life Sci 64, 307–317.
Neukirchen D, Bradke F (2011). Cytoplasmic linker proteins regulate neuronal polarization through microtubule and growth cone dynamics. J Neurosci 31, 1528–1538.
Nishimura Y, Applegate K, Davidson MW, Danuser G, Waterman CM (2012). Automated screening of microtubule growth dynamics identifies MARK2 as a regulator of leading edge microtubules downstream of Rac1 in migrating cells. PLoS One 7, e41413.
Otsu N (1979). A threshold selection method from gray-level histograms. IEEE Trans Syst Man Cybern 9, 62–66.
Park EC, Lee H, Hong Y, Kim MJ, Lee ZW, Kim SI, Kim S, Kim GH, Han JK (2012). Analysis of the expression of microtubule plus-end tracking proteins (+TIPs) during *Xenopus* laevis embryogenesis. Gene Expr Patterns 12, 204–212.
Patel K, Nogales E, Heald R (2012). Multiple domains of human CLASP contribute to microtubule dynamics and organization in vitro and in *Xenopus* egg extracts. Cytoskeleton 69, 155–165.
Rajnicek AM, Foubister LE, McCaig CD (2006). Growth cone steering by a physiological electric field requires dynamic microtubules, microfilaments and Rac-mediated filopodial asymmetry. J Cell Sci 119, 1736–1745.
Riedl J *et al*. (2008). Lifeact: a versatile marker to visualize F-actin. Nat Methods 5, 605–607.
Rogers SL, Wiedemann U, Hacker U, Turck C, Vale RD (2004). Drosophila RhoGEF2 associates with microtubule plus ends in an EB1-dependent manner. Curr Biol 14, 1827–1833.
Sabry JH, O'Connor TP, Evans L, Toroian-Raymond A, Kirschner M, Bentley D (1991). Microtubule behavior during guidance of pioneer neuron growth cones in situ. J Cell Biol 115, 381–395.
Sbalzarini IF, Koumoutsakos P (2005). Feature point tracking and trajectory analysis for video imaging in cell biology. J Struct Biol 151, 182–195.
Sousa A, Reis R, Sampaio P, Sunkel CE (2007). The *Drosophila* CLASP homologue, Mast/Orbit regulates the dynamic behaviour of interphase microtubules by promoting the pause state. Cell Motil Cytoskeleton 64, 605–620.
Stepanova T, Slemmer J, Hoogenraad CC, Lansbergen G, Dortland B, De Zeeuw CI, Grosveld F, van Cappellen G, Akhmanova A, Galjart N (2003). Visualization of microtubule growth in cultured neurons via the use of EB3-GFP (end-binding protein 3-green fluorescent protein). J Neurosci 23, 2655–2664.
Stepanova T *et al*. (2010). History-dependent catastrophes regulate axonal microtubule behavior. Curr Biol 20, 1023–1028.
Strasser GA, Rahim NA, VanderWaal KE, Gertler FB, Lanier LM (2004). Arp2/3 is a negative regulator of growth cone translocation. Neuron 43, 81–94.
Straube A, Merdes A (2007). EB3 regulates microtubule dynamics at the cell cortex and is required for myoblast elongation and fusion. Curr Biol 17, 1318–1325.
Suter DM, Schaefer AW, Forscher P (2004). Microtubule dynamics are necessary for SRC family kinase-dependent growth cone steering. Curr Biol 14, 1194–1199.
Tanaka E, Ho T, Kirschner MW (1995). The role of microtubule dynamics in growth cone motility and axonal growth. J Cell Biol 128, 139–155.
Tanaka E, Kirschner MW (1995). The role of microtubules in growth cone turning at substrate boundaries. J Cell Biol 128, 127–137.
Tanaka EM, Kirschner MW (1991). Microtubule behavior in the growth cones of living neurons during axon elongation. J Cell Biol 115, 345–363.
Tsvetkov A, Popov S (2007). Analysis of tubulin transport in nerve processes. Methods Mol Med 137, 161–173.
Van der Vaart B, Akhmanova A, Straube A (2009). Regulation of microtubule dynamic instability. Biochem Soc Trans 37, 1007–1013.
Waterman-Storer CM, Salmon ED (1998). How microtubules get fluorescent speckles. Biophys J 75, 2059–2069.
Wörz S, Sander P, Pfannmoller M, Rieker RJ, Joos S, Mechtersheimer G, Boukamp P, Lichter P, Rohr K (2010). 3D geometry-based quantification of colocalizations in multichannel 3D microscopy images of human soft tissue tumors. IEEE Trans Med Imaging 29, 1474–1484.
Zack GW, Rogers WE, Latt SA (1977). Automatic measurement of sister chromatid exchange frequency. J Histochem Cytochem 25, 741–753.
Zhou FQ, Cohan CS (2004). How actin filaments and microtubules steer growth cones to their targets. J Neurobiol 58, 84–91.

Supplemental data Marx et al.

Table 1: Plus-end velocities decrease prior to transition to pause or catastrophe in the growth cone.

	>30 sec before catastrophe	30-15 sec before catastrophe	last 15 sec before catastrophe
Number of tracks in growth cone	240	390	390
Comet velocity in growth cone (%)	97.9 ±2.4	100.0 ±2.1	88.7±2.2
Number of tracks in shaft	101	155	155
Comet velocity in shaft (%)	99.0 ± 3.3	100.0 ± 3.8	96.2 ±3.1

Table 1: Relative comet velocities of tracks divided into different phases. EB3 comet velocities were normalized to the average velocities of all tracks in growth cone or shaft of the period 30-15 seconds before catastrophe and are shown with relative s.e.m. calculated from all tracks analyzed.

Table 2: Decreased pioneer microtubules enter filopdia in XCLASP1-depleted neurons.

	Tracks in filopodia	Tracks in growth cone*	Proportion of tracks in filopodia per growth cone ± s.e.m	Number of growth cones
Non-injected	131	1184	0.14 ±0.052	21
Control MO	192	853	0.18 ±0.098	17
XCLASP1 MO	91	1084	0.16±0.045	28

Table 2. Automatic separation of tracks in filopdial verus growth cone interior tracks.

*tracks in growth cone but not in filopdia

Supplemental Figures

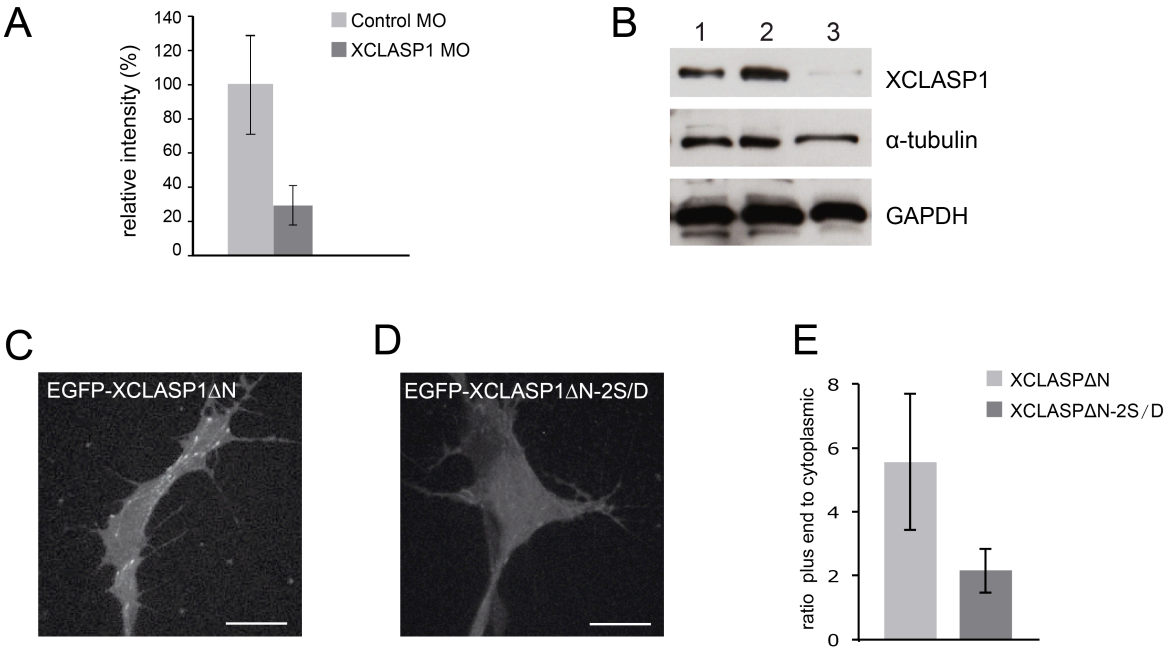

Supplemental Figure 1. XCLASP1 depletion in *Xenopus* and analysis of MT-binding. (A) Quantification of XCLASP1 depletion by XCLASP1 MO in *Xenopus leavis* growth cones by immunocytochemistry using an affinity purified XCLASP1 antibody (Xorbit antibody, Hannak and Heald, 2006). The average intensity in the growth cone of control MO was normalized to 100%. (B) Morpholino based XCLASP1 knockdown in Xenopus laevis kidney epithial cell line analyzed by Western analysis with XCLASP1 antibody. 1: wt; 2: control MO; 3: XCLASP1 MO. (C-E) Analysis of plus-end binding of XCLASP with spinning disk confocal microscopy in growth cones. EGFP-XCLASPΔN shows plus-end tracking (C) while EGFP-XCLASP1ΔN-2SD shows only very reduced plus-end tracking and more cytoplasmic localization. (E) Quantitation of plus-end binding as ratio of plus-end to cytoplasmic intensity in XCLASPΔN and XCLASPΔN-2SD expressing growth cones. Error bars represent standard deviation.

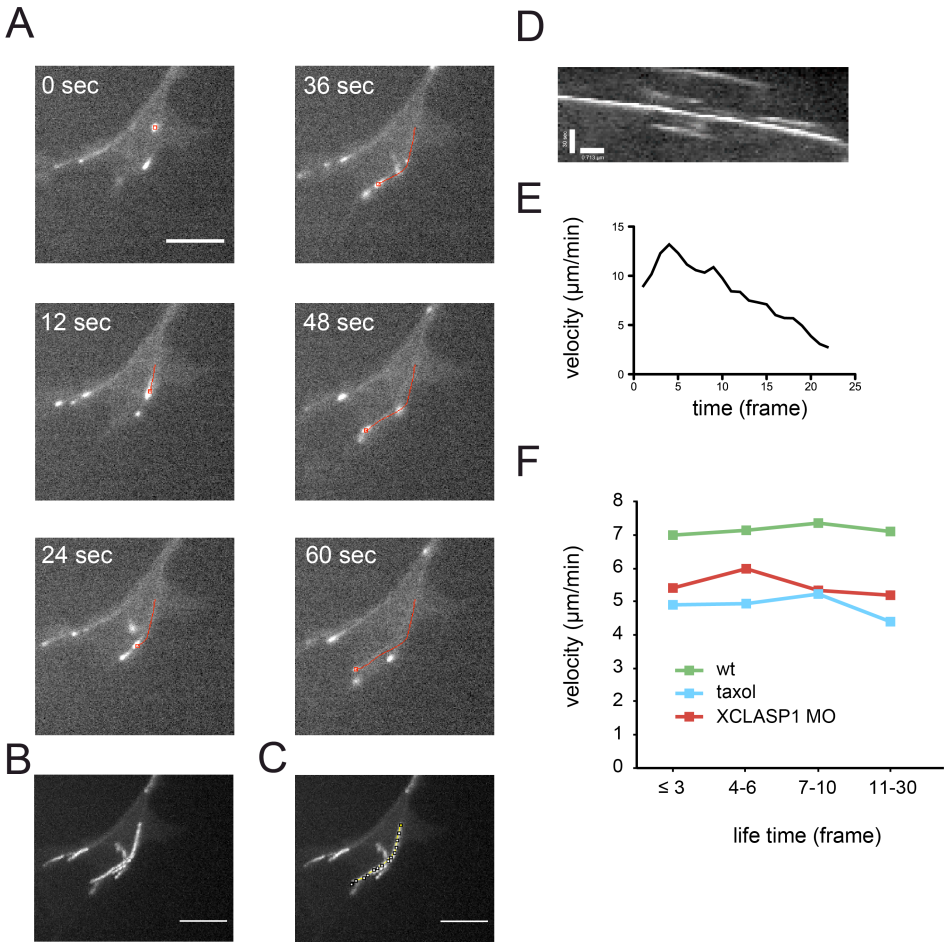

Supplemental Figure 2. Comparison of kymograph analysis with automated tracking of EB3 comets. (A) Automated tracking of EB3-EGFP. The trajectory (red) of the growing microtubule plus-end is shown superimposed with the original image sequence. (B) Maximum intensity projection of frames shown in a. (C) Superimposition of manually tracking of trajectory (yellow). Scale bar: 5 µm. (D) Kymograph along trajectory shown in (C). (E) Plot of instantaneous velocities over time reveals decrease of velocity as the MT plus-end advances into periphery. (F) Relation between lifetime (frames) and instantaneous velocity of wt, XCLASP1 MO injected neurons and neurons treated with 7 nM taxol. Frame rate was one image every 3 seconds.

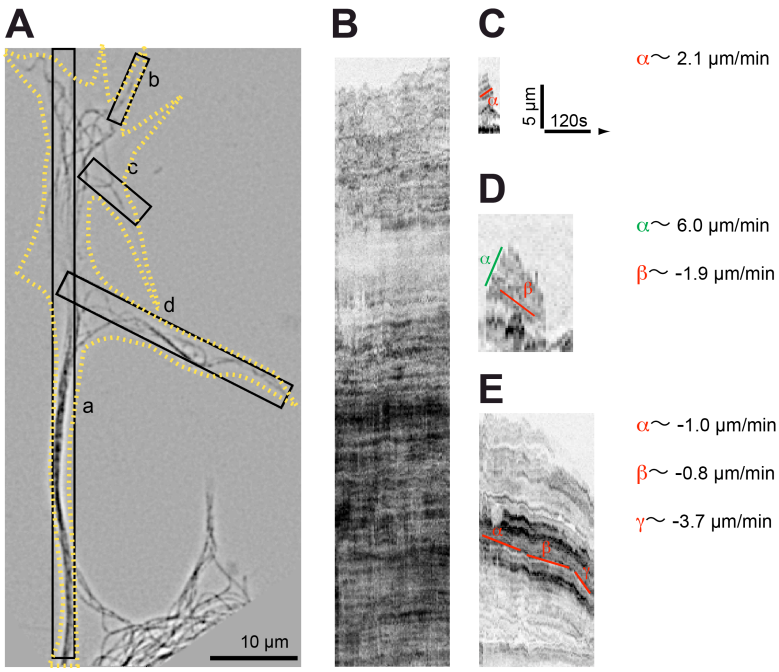

Supplemental Figure 3. MTs in the growth cone undergo positive and negative transport. (A-E) Tubulin speckle microscopy in spinal cord growth cone. Speckles of HiLyte488-tubulin are shown intensity-inverted. (A) MT polymer labeled with low concentrations of conjugated tubulin shows vague outline of MTs (approximate growth cone outline indicated by broken yellow line) (B) Kymograph analysis in region a (see A). The almost horizontal lines indicate very weak anterograde bulk transport. (C) Kymograph analysis in region b (see A) in a growing filopodium with anterograde tubulin flow (red line). (D) Kymograph analysis in region c, where a single MT advances and then retracts. The green line shows plus-end advance, the red line retrograde movement of the MT. (E) Kymograph analysis in region d in a filopodial branch that retracts. The red lines indicate different phases of MT polymer transport in the direction of the axonal shaft.

Supplemental Material and Methods

Immunofluorescence and in-situ hybridization

Neuronal cultures were fixed with icecold Methanol,1 mM EGTA for 20 min at -20°C, then blocked 30 min with 5% normal goat serum (SIGMA-Aldrich) in PHEM (60 mM PIPES, 25 mM HEPES, 10 mM EGTA, 2 mM $MgCl_2$, pH 6.9) at room temperature. Primary antibodies were incubated 2 hours at room temperature in 5% goat serum in PHEM. Washing was performed 3 times with PHEM followed by incubation of secondary antibodies 1 hour at room temperature in 5% normal goat serum in PHEM. After washing 3 times with PHEM, images were recorded. Antibody combinations were Primary antibodies were mouse antibody anti-EB1 (1:200, BD Biosciences) and monoclonal rat anti-tyrosine-tubulin YL 1/2 (1:500, Millipore) detected with the secondary antibodies preabsorbed goat anti-mouse Cy3 and goat anti-rat Cy5 (Jackson ImmunoResearch Laboratories Inc., 1:300), Xorbit antibody 1:1000, detected by anti-rabbit Alexa-Fluor 488 1: 400 (Invitrogen). For detection of f-actin with phalloidin-Atto565 (SIGMA), growth cones were fixed in 4% paraformaldehyde in Krebs buffer (Dent and Kalil, 2001) for 10 minutes. After washing with PHEM phalloidin was added directly, or samples were incubated in 0.5% Triton-X in PHEM for 30 minutes and immuno-stained with DM1α (SIGMA, 1:500), with the phalloidin added with the secondary antibody (anti-rabbit Alexa-Fluor 488, 1:500).
Stage 28 embryos were fixed in 1x MEMFA containing 3.7% formaldehyde for in-situ hybridization. The XCLASP1 in-situ probes were transcribed with T7 (anti-sense) and Sp6 (sense) on pCMV-SPORT6 after linearization of the plasmid with EcoRI (anti-sense) and XhoI (sense). Whole mount hybridization was performed as described in (Gawantka *et al*., 1995).

Microscopy of fixed specimen:

Immunofluorescence was evaluated on a Nikon TiE equipped with a 60x TIRF Apo NA 1.49 objective using a Orca AG CCD camera (Hamamatsu) or with a Perkin Elmer spinning disk confocal system with a Yokogawa CSU-22 and a Nikon 100x PlanApo NA 1.4 objective (Figure 8A-C). For super-resolution imaging (Figure 9) a Nikon N-SIM with a 100x TIRF Apo NA 1.49 with a 3-dimensional patterned illumination was used. To reconstruct super-resolution images, 5 phases and 3 orientations were collected in a single plane onto a Andor Xion DU-897 Electron Multiplier CCD charged coupled device (EM-CCD). A 2.5x magnification was mounted in front of the camera to achieve sampling at 64 nm pixel size. Control MO and XCLASP1 MO positive neurons were identified by dextran Alexa Fluor 647 (Invitrogen).

Western analysis

Proteins were immobilized from SDS Page gel on nitrocellulose membrane by Western blotting. The membrane was then blocked with 5 % milk powder, 0.1 % Tween 20 in PBS and then incubated with rabbit-XCLASP1 antibody (1:200), monoclonal anti-tubulin DM1A (1: 1000, Sigma-Aldrich) and monoclonal GAPDH 6C5 antibody (1:1000, Merck). The membrane was washed with 0.1 % Tween 20 in PBS and the secondary antibodies were added at 1:5000 dilution (goat anti-rabbit horseradish peroxidase and goat anti-mouse horseradish peroxidase, Jackson ImmunoResearch Laboratories Inc.). Then the membrane

was washed again and incubated with ECL Western Blot solution before the signal was detected with a light sensitive film.

XCLASP1 knock down in *Xenopus* cell culture

XCLASP1 knock down was performed in XLKE cells (*Xenopus laevis* kidney epithelial cells) growing in medium containing 60% DMEM 4.5 g/l Glucose (PAA Laboratories GmbH), 10% FCS (PAA Laboratories GmbH), 1% penicillin/streptomycin, 29% H2O at 25°C and 37% CO2. At 90% confluency, 3 μM morpholino oligonucleotide and 6 μM Endo-Porter (Gene Tools LLC) were added. Cells were incubated for two days before cells were washed once with PBS, before being lysed with NP-40 buffer (40 mM Tris pH 7.5, 5 mM EDTA, 0.5% NP-40, 150 mM NaCl and protease cocktail). The solution was incubated 30 min on ice before being centrifuged. After measuring protein concentration, the supernatant was mixed with SDS loading dye and heated before being analyzed on SDS Page gel. For each lane 10.6 μg protein was loaded.

Supplemental references

Gawantka, V., Delius, H., Hirschfeld, K., Blumenstock, C., and Niehrs, C. (1995). Antagonizing the Spemann organizer: role of the homeobox gene Xvent-1. Embo J. *14*, 6268-6279.

Hannak, E., and Heald, R. (2006). Xorbit/CLASP links dynamic microtubules to chromosomes in the Xenopus meiotic spindle. J. Cell Biol. *172*, 19-25.

Movies:

Movie 1: Timelapse sequence of EGFP-XCLASP1ΔN in *Xenopus* spinal cord growth cone.

Movie 2: EB3-mCherry comet imaging in *Xenopus* spinal cord neurons for tracking of MT ends. Analysis of this time lapse sequence is shown in Figure 2 and Figure 5.

Movie 3: EB3-EGFP comet movement in *Xenopus* spinal cord neurons treated with 3.3 nM Taxol. Microtubule dynamics are attenuated, but EB3 still binds to plus-ends.

Movie 4: EB3-EGFP and Liveact-EGFP in *Xenopus* spinal cord neurons for simultaneous tracking of MT ends and F-actin. Analysis of this time-lapse sequence is shown Figure 5.

Movie 5: Visualization of MT plus end velocities in movie 2. The color added at each frame relates to the average velocity of neighboring frames.

Movie 6: EB3-mCherry comet imaging in *Xenopus* spinal cord neurons for tracking of MT ends in proximal and distal shaft. Analysis of this timelapse sequence is shown in figure 5, K and J.

Movie 7: Wild type neuron expressing Lifeact-EGFP (shown intensity inverted).

Movie 8: Control MO-injected neuron expressing Lifeact-EGFP (shown intensity inverted).

Movie 9: XCLASP1 MO-injected neuron expressing Lifeact-EGFP (shown intensity inverted).